Key Points:
- 86% of AR events in the western U.S. is related to three trajectory types
- Precipitation of given AR events is strongly determined by the trajectory types
- Trajectory types are linked to diabatic and upper-level PV anomalies

Correspondence to:
J.-M. Ryoo,
ju-mee.ryoo@nasa.gov

Classification of atmospheric river events on the U.S. West Coast using a trajectory model

Ju-Mee Ryoo[1], Duane E. Waliser[2,3], Darryn W. Waugh[4], Sun Wong[2], Eric J. Fetzer[2], and Inez Fung[5]

[1]Atmospheric Science Branch, NASA Ames Research Center, Moffett Field, California, USA, [2]Jet Propulsion Laboratory, California Institute of Technology, Pasadena, California, USA, [3]Joint Institute for Regional Earth System Science and Engineering/Department of Atmospheric and Oceanic Sciences, University of California, Los Angeles, California, USA, [4]Department of Earth and Planetary Sciences, Johns Hopkins University, Baltimore, Maryland, USA, [5]Department of Earth and Planetary Sciences, University of California, Berkeley, California, USA

Abstract We investigate transport pathways of water vapor associated with landfalling atmospheric river (AR) events that result in precipitation along the West Coast of the U.S. for winters of 1997–2010. The water vapor transport pathways are determined by computing back trajectories with a trajectory model using the Modern Era Retrospective analysis for Research and Applications reanalysis data set. The majority of AR events (86%) over the West Coast of the U.S. are grouped into three trajectory types, and two of them are closely associated with the AR events. We designate the first type as Ascending near landfall and of Tropical Origin (AT), the second type as Ascending near landfall and of Extratropical Origin (AE), and the third type as Descending or parallel near landfall and of Extratropical Origin (DE), which is accompanied but not directly associated with the AR events. The magnitude and spatial distribution of precipitation of a given AR event are found to be strongly determined by the type of trajectories. In general, AR events composed of both AT and AE trajectories have more frequent precipitation over a broad region of the western U.S. and AR events composed of both AT and DE trajectories have intense precipitation over the southwestern U.S. due to AT trajectories. AR events of AT-only trajectories have intense precipitation, especially over the northwestern U.S., but are less frequent compared to those of AT + AE trajectories. In addition, different patterns of trajectory types among AR events are closely linked to upper level potential vorticity (PV) anomalies; 66% of AR events are associated with anticyclonic Rossby wave breaking events.

1. Introduction

It has been expected that extreme precipitation episodes will be more frequent and more intense as the climate changes [*Jain et al.*, 2005; *Dettinger*, 2011]. The large interannual variability in U.S. West Coast precipitation in recent years has presented a challenge to water resource managers. Thus, the effort to gain a better understanding of the origins of precipitation and its moisture pathways has also increased. Development of satellite-based remote sensing techniques enables us to confirm that extreme precipitation over the West Coast of the U.S. often coincides with transport in deep and narrow corridors of concentrated water vapor originating over the ocean, commonly referred to as "atmospheric rivers" (ARs) [*Newell et al.*, 1992; *Zhu and Newell*, 1994; *Kerr*, 2006; *Ralph et al.*, 2004, 2006; *Knippertz and Martin*, 2007; *Neiman et al.*, 2008; *Dettinger et al.*, 2011; *Newman et al.*, 2012]. *Knippertz and Martin* [2007] show that for some cases of extratropical cyclones making landfall with heavy precipitation on the U.S. West Coast, a band of large integrated water vapor (IWV) is observed extending to the south, implying that a large amount of moisture is directly transported from the tropics. However, based solely on satellite images of IWV, it is not obvious where the moisture originates or what pathways it follows.

Tracing parcel histories can determine where air parcels originate and provide a time record of thermodynamic conditions experienced by the air parcels. *Bao et al.* [2006] performed a trajectory analysis using a regional mesoscale model and related trajectories from the Tropics with high-IWV bands over the eastern North Pacific. *Knippertz and Wernli* [2010] also calculated water vapor flux from a Lagrangian trajectory model by interpolating the model fields at a given time to identify the tropical moisture export. These studies put more emphasis on the role of the direct moisture transport from the tropics. While the narrow and long bands of moisture plumes often develop in association with equatorward filaments connected to extratropical cyclones in a baroclinic wave system [*Zhu and Newell*, 1998; *Couhert et al.*, 2010], there is also evidence that such bands

evolve and move with the development of extratropical cyclones and storm track [*Lackmann and Gyakum*, 1999; *Neiman et al.*, 2008]. *Dettinger et al.* [2011] mentioned that in central and northern California, the contributions of large "pineapple express" precipitation (i.e., those emanating from the tropics), as a subset of ARs, tend to be associated with southern displacements of the storm tracks over the midlatitude Pacific and enhancement of the subtropical jet over the North Pacific basin. In a related study, *Newman et al.* [2012] showed that transient eddies play an important role in transporting moisture associated with latent heating from the tropics into the extratropics and the West Coast of the U.S., highlighting that much of low-frequency transport is of extratropical origin. These studies suggest multiple water vapor pathways for ARs, and even hint at the possibility that tropical AR air parcels may merge with AR air parcels from the extratropics.

There are also several studies that relate the extreme precipitation events with upper level disturbances. [*Appenzeller and Davies*, 1992; *Lackmann*, 2002; *Eckhardt et al.*, 2004; *Martius et al.*, 2006; *Madonna et al.*, 2014; *Massacand et al.*, 1998], although those studies do not directly refer to the phenomenon as "AR" events. AR events, the enhanced water vapor bands making landfall along the West Coast of North America as well as other continents [*Zhu and Newell*, 1994, 1998; *Waliser et al.*, 2012], are often observed along relatively narrow regions within the "warm conveyor belt" [*Knippertz and Martin*, 2007; *Neiman et al.*, 2008; *Knippertz and Wernli*, 2010; *Joos and Wernli*, 2012; *Pfahl et al.*, 2014] associated with a cold front. Considering that the characteristic patterns in a developing baroclinic system are ascending motion of warm surface air near the warm conveyor belt, along with descending motion in the dry intrusion from the upper level [*Polvani and Esler*, 2007], the AR events can be affected by the upper level disturbances.

Upper level potential vorticity (PV) is a typical cause of upper level disturbances. The dynamics of PV and its relation to relative humidity (RH) and precipitation have been studied through National Centers for Environmental Prediction (NCEP)-National Center for Atmospheric Research Reanalysis, rain gauge data, trajectories, and satellite observations such as Total Ozone Mapping Spectrometer and Atmospheric InfraRed Satellite data [*Wernli and Davies*, 1997; *Lackmann and Gyakum*, 1999; *Massacand et al.*, 2001; *Waugh*, 2005; *Ryoo et al.*, 2008, 2013; *Martínez-Alvarado et al.*, 2014]. *Waugh* [2005] showed that upper level PV often originates within dry and cold stratospheric air to the west of high PV intrusions by promoting downward motions and brings moist and warm tropospheric air to the east of high PV intrusions by inducing strong upward motions. It has been also found that PV intrusions from the (subtropical) upper troposphere into the lower troposphere reduce static stability and initiate convection with strong ascent at the leading edge of high PV [*Waugh and Funastu*, 2003; *Funatsu and Waugh*, 2008]. Using trajectory analysis, *Wernli and Davies* [1997] and *Massacand et al.* [2001] showed that a midlevel diabatic heating maximum induces negative upper level PV anomalies and that this can be a feature of cyclogenesis events. *Joos and Wernli* [2012] also found that a warm conveyor belt modifies the upper level PV by producing a positive low-level PV anomaly. *Lackmann and Gyakum* [1999] found that diabatic heating produces the lower cyclonic PV maximum that drives the low-level jet, and above the heating maximum, an anticyclonic PV anomaly forms in response. *Ryoo et al.* [2013] reported that precipitation locations and timing over the West Coast of the U.S. can be closely linked to the locations and types of PV intrusions (different phases of Rossby wave breakings), which implied that heavy precipitation events such as ARs can be affected by the position of PV. Very recently, *Martínez-Alvarado et al.* [2014] also examined the warm conveyor belts and related them to the upper level PV anomalies and wave breaking features using numerical model simulations. Therefore, understanding the patterns and frequencies of upper level wave breaking events such as "potential vorticity (PV) intrusions" may help to understand the location and intensity of heavy precipitation events such as ARs.

In this study, the dominant water vapor transport pathways for ARs impacting the U.S. West Coastal region are examined using cluster analysis on Lagrangian back trajectory simulations. In addition, composite analyses are used to determine how the overland precipitation intensity and spatial characteristics, as well as the associated large-scale circulation characteristics, depend on the dominant AR trajectories. This study also briefly examines how ARs and PV are related.

2. Methodology

2.1. AR Events

Neiman et al. [2008] employed a composite of Special Sensor Microwave/Imager (SSM/I) (and later Special Sensor Microwave Imager/Sounder (SSMIS)) sensors on multiple satellites. The AR events used in our study are an

extension of events in *Neiman et al.* [2008] and cover 1997 to 2010 (the dates after those reported in *Neiman et al.* [2008] were obtained from P. Neiman (personal communication, 2010)). The events are defined using SSM/I and the criterion of integrated water vapor being larger than 2 cm in either the morning or afternoon passes of the satellite. All AR events that have landfall over the U.S. West Coast (California to Washington coasts) during the winter (December–March) are analyzed, although four AR events (13 March 2003; 11 December 2004; 22 March 2005; and 16 February 2009) from *Neiman et al.* [2008] were excluded from the analysis due to computation errors in calculating their trajectory clusters. This left a total of 140 AR events for the analysis. More information about trajectories and classification of trajectories for AR events will be discussed below.

2.2. Trajectory Model

Back trajectory calculations in this study are performed using the NASA Goddard Fast Trajectory Model. This model was developed by *Schoeberl and Sparling* [1995] and later modified by *Wright et al.* [2011] and *Huang et al.* [2012]. The parcel history (trajectory) $X(t)$ is calculated by integration of the equation $DX(t)/Dt = U(t)$, where $X(t)$ is the location (longitude, latitude, and potential temperature) of the air parcel and $U(t)$ is the three dimensional wind velocity (with diabatic heating rate as the vertical velocity). The trajectories are determined using the Global Modeling and Assimilation Office Modern Era Retrospective analysis for Research and Applications (MERRA) reanalysis fields [*Suarez et al.*, 2008; *Bosilovich et al.*, 2008, 2011; *Rienecker et al.*, 2011]. The MERRA horizontal winds and temperatures are reported at a horizontal resolution of 0.66° longitude by 0.5° latitude on 42 pressure levels spanning from 1000 to 0.01 hPa, and 6-hourly time resolution. Diabatic heating rates are reported on the reduced resolution (1.25° × 1.25°) over 3-hourly time resolution. See *Bosilovich et al.* [2008] for additional information regarding the MERRA reanalysis. All fields are vertically interpolated to a potential temperature grid and are also interpolated linearly in time and space to the trajectory location at each time step of the trajectory integration. A fourth-order Runge–Kutta method is used to calculate trajectory motion, and it is calculated for every 28 min time step (i.e., 50 time steps per day).

The region 125°W–115°W, 34°N–50°N, the West Coast of the U.S., is used as the target region for calculating back trajectories. AR landfalls in this region are important as they impact the precipitation, water resources, and floods, and play a key role this region's snowpack—critical to the regional water availability [*Grubišić et al.*, 2005; *Soong and Kim*, 1996]. For each AR event, back trajectory calculations are started from a regular longitude-latitude grid with spacing of 1.25° covering 125°W–115°W, 34°N–50°N (see the grid box in Figure 3), resulting in 117 trajectories per event. Thus, the total number of trajectories used in the clustering analysis is 16,380 (117 × 140 AR events).

All trajectories are released at a potential temperature of 290 K (1000–700 hPa, 0–3 km in the midlatitude). The levels below 3 km are chosen for the back trajectory calculation because (i) 1 km above the surface is typically the level where significant moisture is transported via the strong low-level jet within the warm conveyor belt and IWV band, resulting in strong horizontal water vapor fluxes [*Ralph et al.*, 2004; *Bao et al.*, 2006], and (ii) the region up to 2–3 km above the surface encompasses the region of most of the moisture making up the strong moisture signature of the IWV band, or atmospheric river, which is a result of the ascent of moist air forced by the cold front [*Browning*, 1986; *Bao et al.*, 2006]. Additional support for this choice of levels for the trajectory release comes from *Ralph et al.* [2005], who showed that about 75% of the water vapor transport within ARs occurs within the lowest 2.5 km of the atmosphere. Trajectories are calculated backward from the targeted time of each AR event for 5 days, a typical timescale of water vapor transport associated with synoptic-scale systems [*Roca et al.*, 2005; *Moncrieff et al.*, 2007]. Tests using meteorological fields from NCEP [*Kalnay et al.*, 1996] or European Centre for Medium-Range Weather Forecasts [*Simmons et al.*, 2007] for several extreme AR precipitation events show no significant differences from calculations using MERRA for trajectories in our region of interest [*Ryoo et al.*, 2010] although more detailed analysis remains to be explored in terms of the difference of daily diabatic heating and model physics in various regions among different reanalysis data sets.

2.3. Clustering Method

We identify the transport pathways associated with the AR events over the western U.S. by clustering trajectories using the *K*-means algorithm. The algorithm starts with a specified number (*K*) of random clusters and then iteratively assigns trajectories to clusters to minimize the variation of trajectory locations within each cluster while maximizing the variation of trajectory locations between clusters. To classify trajectories we use all three spatial coordinates (longitude and latitude (in degrees), and height (in meters)). *Fernau and*

Samson [1990] and *Dorling et al.* [1992] ignored the vertical transport when constructing trajectory clusters, while *Cape et al.* [2000] also argued that the horizontal coordinates are more important than the vertical coordinate in defining clusters. However, in this study, the results indicate that vertical motion plays a dominant role in the association between the pathways and the precipitation characteristics over the western U.S.; hence, the vertical component is considered for clustering back trajectories as in *Ryoo* [2009].

We applied K-means clustering with $K = 2$ (two clusters) to the 117 trajectories for each AR event and repeated it for all 140 AR events. This allows us to characterize the pathways for each event and then subsequently consider whether common water vapor pathways exist among the different events. We chose $K = 2$ as the preliminary analysis showed that for most events the trajectories could be separated into two groups: those with either tropical or extratropical origin.

3. Trajectory Pathways

3.1. Illustrative Examples

Figure 1 shows an example of the horizontal and vertical trajectory patterns to the target region for three AR events: 19 January 2005; 14 January 1998; and 16 February 2004. This shows that while there are groups (clusters) of parcels with the same trajectories within each event, there are differences between events. For 19 January 2005 (Figures 2a and 2b), the trajectories mostly come from the lower tropical region with ascent near the western U.S., a typical type of AR event often called the pineapple express [e.g., *Ralph et al.*, 2004]. For 14 January 1998 (Figures 2d and 2e) the trajectories originate in either the lower altitude tropics or the midtroposphere extratropical Pacific, with both types ascending very near the western U.S. There are also two branches of trajectories for 16 February 2004 event (Figures 2g and 2h), but the characteristics of the extratropical trajectories differ from the 14 January 1998 event—notable is their descent near the western U.S.

As will become evident from the results of the analysis discussed below, the vast majority of the AR events investigated in this study are associated with back trajectories sharing features illustrated by these three events. Furthermore, in order to consider "moist" parcels, we select parcels only if the specific humidity (q) along the trajectories is greater than $1\,g\,kg^{-1}$ at day 0. The classification is not very sensitive to the q threshold chosen. However, the meteorological fields show more similarity within the group with $q > 1\,g\,kg^{-1}$ than with a larger threshold (e.g., $q > 3\,g\,kg^{-1}$). This seems to be due to the fact that trajectories having extratropical origin (such as AE and DE) are filtered out when using a large q threshold. By setting q to a small value, we can effectively remove the dry parcels as well as consider the background systems without losing too much information. Using this criterion, the trajectories during AR events can be classified as one of three types: (i) Trajectories that originate from the lower troposphere of the tropical central eastern Pacific (~170°E–130°W, south of 35°N, below 700 hPa (~3 km)) and undergo ascent near the target region with q larger than $1\,g\,kg^{-1}$; referred to here as "ascending and of tropical origin" or just "AT." (ii) Trajectories that originate from the extratropics across the Pacific (~100°E–130°W, north of 35°N, above 700 hPa) and undergo ascent near the target region with q larger than $1\,g\,kg^{-1}$ and referred to as "ascending and of extratropical origin" or just "AE." (iii) Trajectories from the same region as the AE, but undergo descent or nearly horizontal motion near the target region with q larger than $1\,g\,kg^{-1}$ and are referred to as "descending and of extratropical origin," or just "DE." The 19 January 2005 event contains AT trajectories, the 14 January 1998 event contains AT and AE trajectories, and the 16 February 2004 event contains AT and DE trajectories.

3.2. Types of Trajectories During AR Events

We find that about 86% of the AR events observed during December–March in 1997–2010 (120 of 140 ARs) are the result of either a combination of AT and AE trajectories (65% or 91 of 140), only AT trajectories (14% or 19 of 140), or a combination of AT and DE trajectories (7% or 10 of 140). The other 20 AR events do not fall into the above types or combinations nor do they account for a single uniform type themselves, i.e., they contain just trajectories of extratropical origin (only AE (seven events) or DE (one event) trajectories), "hybrid" types (horizontally classified into the extratropical origin but vertically coming from lower latitudes) (four events), or just "undetermined" types (eight events) of trajectories.

We focus in the rest of this study on the 120 events that can be classified into one of the three types described above. To satisfy our moist criterion, about 70% of total trajectories (9812 trajectories out of 14040 (117×120 events)) are used in this study. Figure 2 and Table 1 show the results of the cluster analysis and AR trajectory
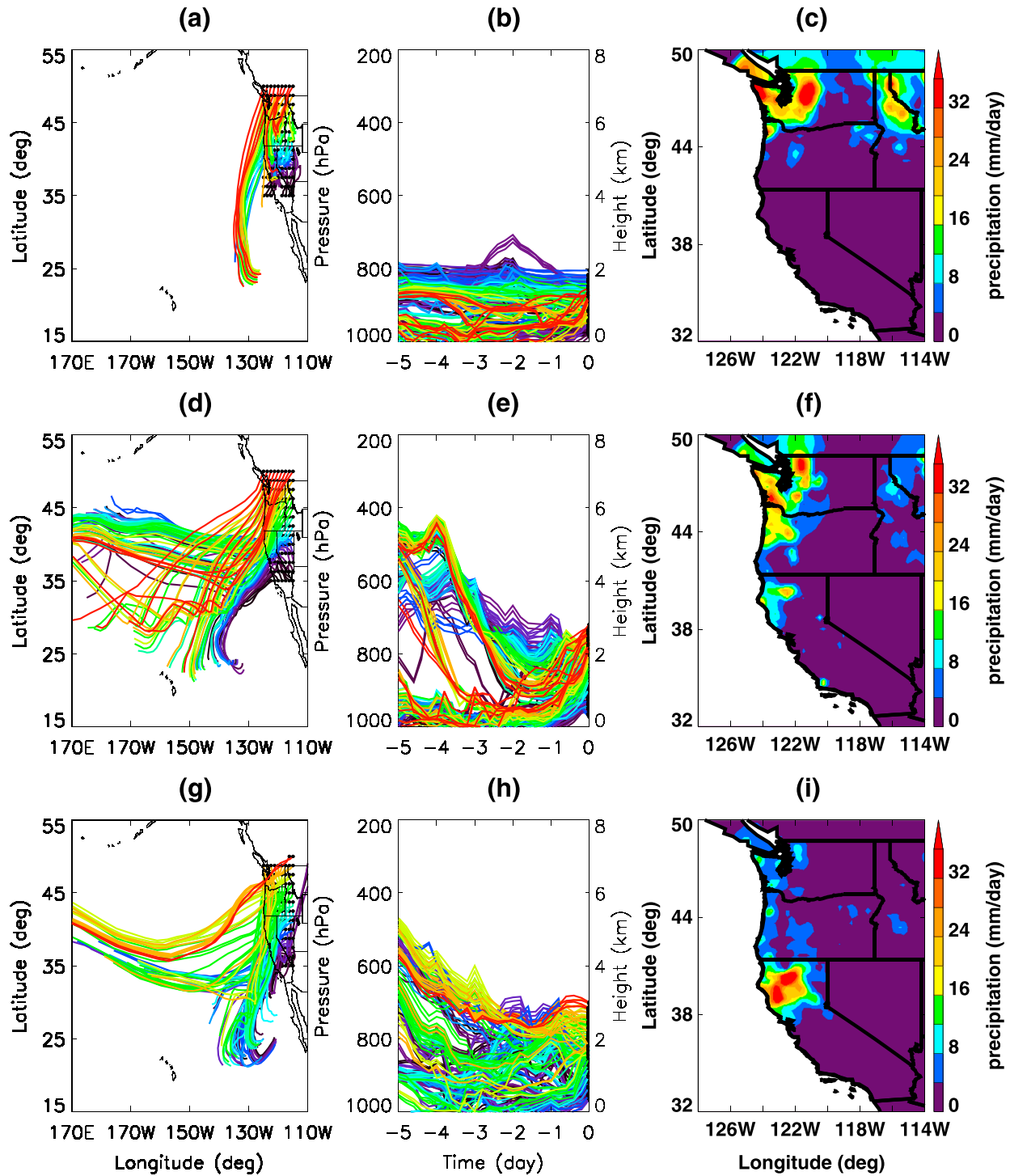
Figure 1. (a, d, and g) horizontal maps, (b, e, and h) vertical evolutions of 5 day back trajectories releasing at 290 K using MERRA reanalysis data set, and (c, f, and i) a map of daily precipitation intensity (unit in mm d^{-1}) for (Figures 1a–1c) 19 January 2005 (AT only), (Figures 1d–1f) 14 January 1998 (AT + AE), and (Figures 1g–1i) 16 February 2004 (AT + DE) AR events. The filled circles in Figures 1a, 1d, and 1g represent the target region (125°W–115°W, 34°N–50°N) where trajectory starts to simulate backward at day 0. Different colors of the trajectories in Figures 1a, 1d, and 1g and Figures 1b, 1e, and 1h represent the individual trajectories ending in different regions. The colors closer to red (blue) signify the trajectories ending at further north (south) within the target region.
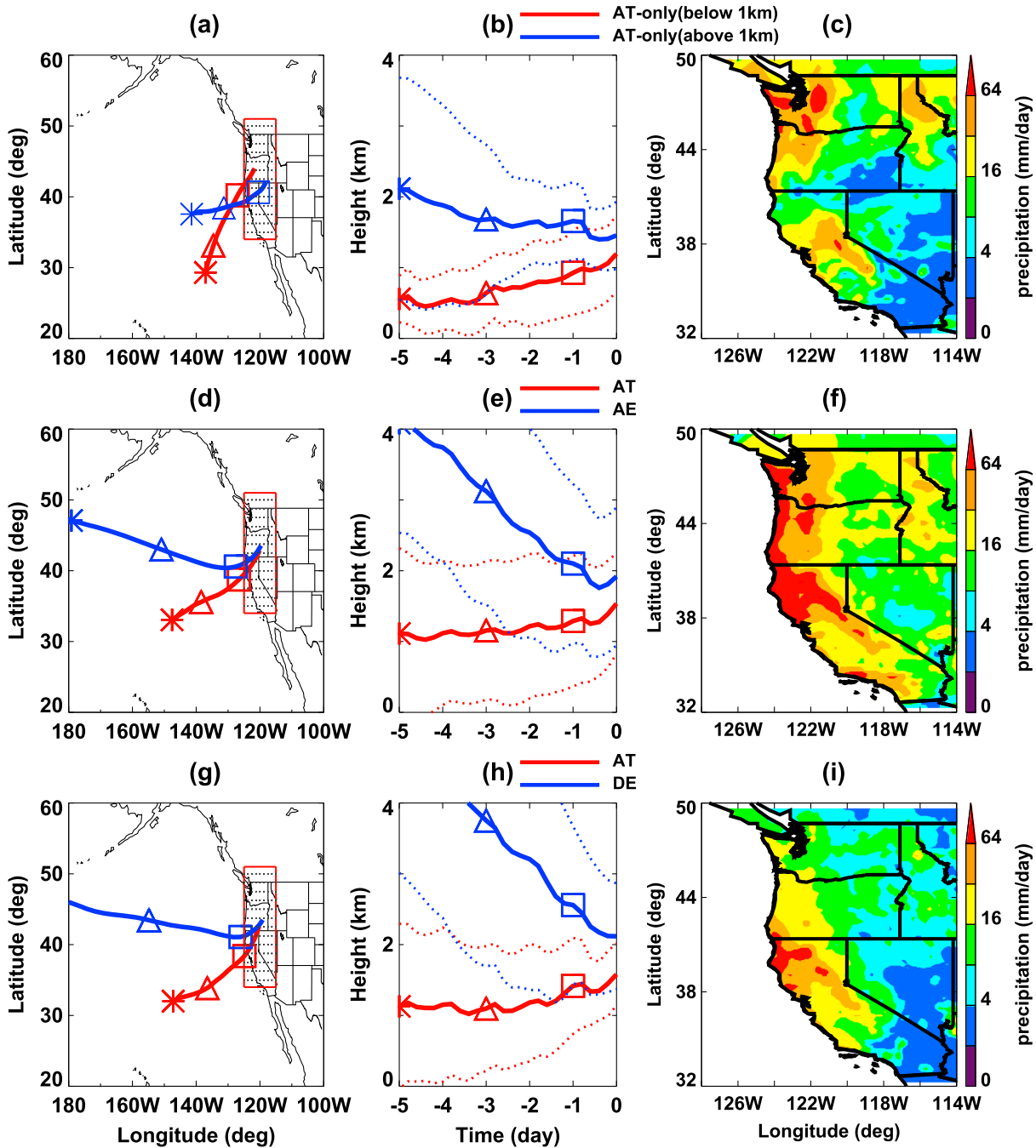
Figure 2. (a, d, and g) Composite mean horizontal maps, (b, e, and h) vertical evolutions of 5 day back trajectories releasing at 290 K using MERRA reanalysis data set, and (c, f, and i) a map of daily precipitation intensity (unit in mm d^{-1}) for (Figures 2a–2c) AT-only, (Figures 2d–2f) AT + AE, and (Figures 2g–2i) AT + DE events. The black dots inside of red box in Figures 2a, 2d, and 2g represent the target region (125°W–115°W, 34°N–50°N) where trajectory starts to simulate backward at day 0. The red solid lines represent the mean trajectories from the tropical origin (AT trajectories) and the blue solid lines represent the mean trajectories from the extratropical origin (AE or DE trajectories). The dashed lines are the 1 standard deviation from the mean. The symbols (squares, triangles, and stars) represent the positions of the trajectory at the time from days −1, −3, and −5, respectively.

characteristics for these events. Table 1 lists the dates of observed AR events sorted into dominant trajectory types, while Figures 2a, 2b, 2d, 2e, 2g, and 2h show the composite mean trajectories of AR events associated with different origins: AT-only, AT + AE, and AT + DE events. The differences in the composite mean trajectory types shown in Figures 2a, 2b, 2d, 2e, 2g, and 2h can be linked to the substantial differences among the composite mean precipitation in Figures 2c, 2f, and 2i, which will be discussed in the next section.

Table 1. Dates of Landfalling AR Events Used in This Study for AT-Only, AT + AE, and AT + DE Events[a]

Types	AT Only		AT + AE		AT + DE
Dates of AR events	19981228	19971205	20030323	20081221	19980202
	19981229	19971216	20030326	20081222	19990227
	19990114	19980114	20031205	20081227	19990325
	20000118	19980115	20031206	20081228	20000124
	20000125	19980126	20031207	20081229	20000305
	20030126	19980205	20031224	20090106	20040216
	20030131	19980322	20041209	20090107	20040217
	20030310	19980323	20050109	20090202	20041208
	20040122	19990110	20050327	20090222	20051201
	20041210	19990115	20051202	20090223	20070122
	20041217	19990207	20051222	20090301	
	20050117	19990224	20051228	20090302	
	20050118	19990324	20051230	20090326	
	20050119	19991216	20051231	20091215	
	20050122	20000116	20060227	20091216	
	20050123	20000117	20060306	20091218	
	20070210	20011229	20060325	20091230	
	20090122	20020102	20061212	20100101	
	20091220	20020106	20061225	20100104	
		20020107	20061226	20100115	
		20020221	20070102	20100118	
		20021212	20070209	20100119	
		20021213	20070311	20100125	
		20021214	20070312	20100126	
		20021216	20071203	20100205	
		20021227	20071204	20100206	
		20030102	20071223	20100214	
		20030112	20080110	20100224	
		20030113	20081206	20100226	
		20030315	20081210	20100312	
				20100329	
Number of events	19		91		10

[a]The dates from December to March in 1997–2005 are obtained from the records of *Neiman et al.* [2008] and those in 2005–2010 are obtained by P. Neiman. AT, AE, and DE refer to trajectories with Ascending near landfall and of Tropical Origin, Ascending near landfall and of Extratropical Origin, and Descending or parallel near landfall and of Extratropical Origin, respectively (see text in more detail). Dates are formatted as yyyymmdd.

3.3. Precipitation and AR Trajectories

We now examine the precipitation over the West Coast of the U.S. during the AR events, and how the precipitation varies between the trajectory types identified above. We use precipitation data obtained from Climate Prediction Center (CPC) $0.25° \times 0.25°$ gridded daily rain gauge analysis [*Higgins et al.*, 2000]. The precipitation intensity associated with a particular trajectory is set as the precipitation from the rain gauge data closest in location and time of the trajectory end (day = 0, when a trajectory starts to run backward).

We first consider the three illustrative events shown in Figure 1. Figures 1c, 1f, and 1i show maps of the daily precipitation amount over the West Coast of the U.S. for each event. The distribution of heavy precipitation varies between the events: In the AT-only event, the region of high precipitation is mostly confined to the central and northern part of the region—with the heaviest centered on Oregon and Washington. In the AT + AE event there is heavy precipitation across along most of the West Coast north of central California, whereas for the AT + DE event precipitation occurs only in a narrow region in southwestern U.S. including California. These distinctions can be related to differences in the trajectories and in particular whether the trajectories ascend or descend. For example, in the AT + AE event, nearly all trajectories ascend as they enter the target region, and there is widespread heavy precipitation. In contrast, in the AT + DE events, only a subset of trajectories ascend, and heavy precipitation occurs in these regions of ascending trajectories, mostly in the southern region.

These three examples suggest that the amount and location of precipitation during AR events will depend on the trajectory type. To examine this further, we analyze the composite mean precipitation for each of the three types of events. The composites of daily precipitation intensities for AT-only, AT + AE, and AT + DE

events are shown in Figures 2c, 2f, and 2i. There are substantial differences among the composite mean precipitation, which can be linked to differences in the trajectories ending in different regions. High-precipitation intensities for the AT-only and the AT + AE events occur over the northern part of coastal and mountainous regions, which are regions with ascending trajectories. In contrast, precipitation intensities are lower especially in the northwestern U.S. for AT + DE events, as there are descending DE trajectories in this region. The coastal and mountainous precipitation in northern California (38–42°N) is related to the elevation of topography. For example, heavy precipitation is observed on the low-elevation coastal regions and the windward side of the mountainous regions (e.g., Sierra Nevada, 37°N–42°N, 124°W–120°W) while light precipitation is observed on the lee side of the mountainous regions (e.g., Sierra Nevada, 37°N–42°N, 120°W–118°W; not shown).

Since the pathways of air parcels would just give us information about short-term air mass transport, we examine the specific humidity (q) along the trajectories in order to represent the pathways of moisture. Figures 3a–3c show the snapshot of the MERRA q for the representative example of AT-only, AT + AE, and AT + DE events, respectively. High water vapor averaged over the surface to 700 hPa clearly extend from the tropics to the West Coast of the U.S. on the given AR event. The mean trajectories show the pathways of air parcels for all categories. For instance, the AT-only trajectories represent well the horizontal and vertical patterns coming from the lower tropics (Figures 3d and 3g). The AT + AE (AT + DE) trajectories also show the spatial patterns of air parcels, coming from the extratropical high altitudes but ending at lower altitudes with upward (downward or parallel) motion at the target region (Figures 3e and 3h for AT + AE, Figures 3f and 3i for AT + DE).

The changes in q along the trajectories are obtained from the nearest points from the MERRA reanalysis (Figures 3j–3l). We interpreted the increase of q as the result of gaining moisture from evaporation of falling precipitation or horizontal mixing and the decrease of q as the result of losing moisture due to precipitation [*Pfahl and Wernli*, 2008; *Pfahl et al.*, 2014]. Other factors, such as errors in the trajectory calculation [*stohl et al.*, 1995], could also play a role but are not examined in this study. Interestingly, the q values associated with the mean trajectories share a number of key characteristics; for example, on 14 January 1998, the q values corresponding to the mean trajectories from the tropics with a lower altitude are larger (maximum up to 13 g kg^{-1} and finally 6 g kg^{-1} at day 0) than those from the extratropics with relatively higher altitudes (maximum up to 8 g kg^{-1} and finally 4.5 g kg^{-1} at day 0) (Figure 3k). The trajectories from the tropics lose a large amount of water vapor during the course of transport until they get to the target regions at day 0, and this appears to be due to significant rainout during the AR event. This rainout along the trajectories represents the heating that is needed to form the diabatic PV maximum which drives the AR [*Lackmann and Gyakum*, 1999]. For trajectories with an extratropical origin such as AE or DE, the trajectories gradually increase their water vapor as they reach low levels in the time window from day − 2 to day 0 (e.g., Figures 3h and 3k and Figures 3i and 3l), even if their initial q is small due to the lack of moisture related to their origin from the extratropics and higher altitudes. This shows that it is likely that a strong moisture source for most of the AR events are in the lower altitude regions, because trajectories from higher altitudes eventually move to lower altitudes near the end (i.e., day 0) in most of the AR events. In order to test the sensitivity of the choice of the trajectory release level, we also computed q along the trajectories ending at 300 K (2–5 km above the surface). The q values calculated along the trajectories ending at 290 K are higher than those at 300 K, and the differences in q between 300 K and 290 K are higher for AE or DE trajectories than AT trajectories (not shown).

A summary of the spatial locations of mean trajectories and their water vapor along the trajectories during the 5 day backward simulation is provided in Table 2 for all AT-only, AT + AE, and AT + DE categories. As seen in the example from Figure 3, the mean water vapors are large for AT only, especially when coming from tropical lower altitudes (AT only (below 1 km): 4.1 g kg^{-1}, AT only (above 1 km): 3.8 g kg^{-1}). For AT + AE, the contribution of both AT and AE is large (AT: 3.7 g kg^{-1}, AE: 3.9 g kg^{-1}). For the AT + DE events, the relative contribution of the AT trajectories for transporting water vapor to the target region is larger than that of DE trajectories (AT: 5.2 g kg^{-1}, DE: 3.2 g kg^{-1}). Note that the contribution of AT trajectories from AT + DE (5.2 g kg^{-1}) is larger than those from AT + AE (3.7 g kg^{-1}), and this indirectly implies that the relatively dry DE trajectories may enhance updraft of warm, moist air from the low altitude carried by AT trajectories. Figure 3 and Table 2 clearly demonstrate the characteristics of the trajectory patterns and the associated water vapor along the trajectories; the trajectories reach a low level (below 850 hPa) near the final reference time (day − 2 to 0), follow northward
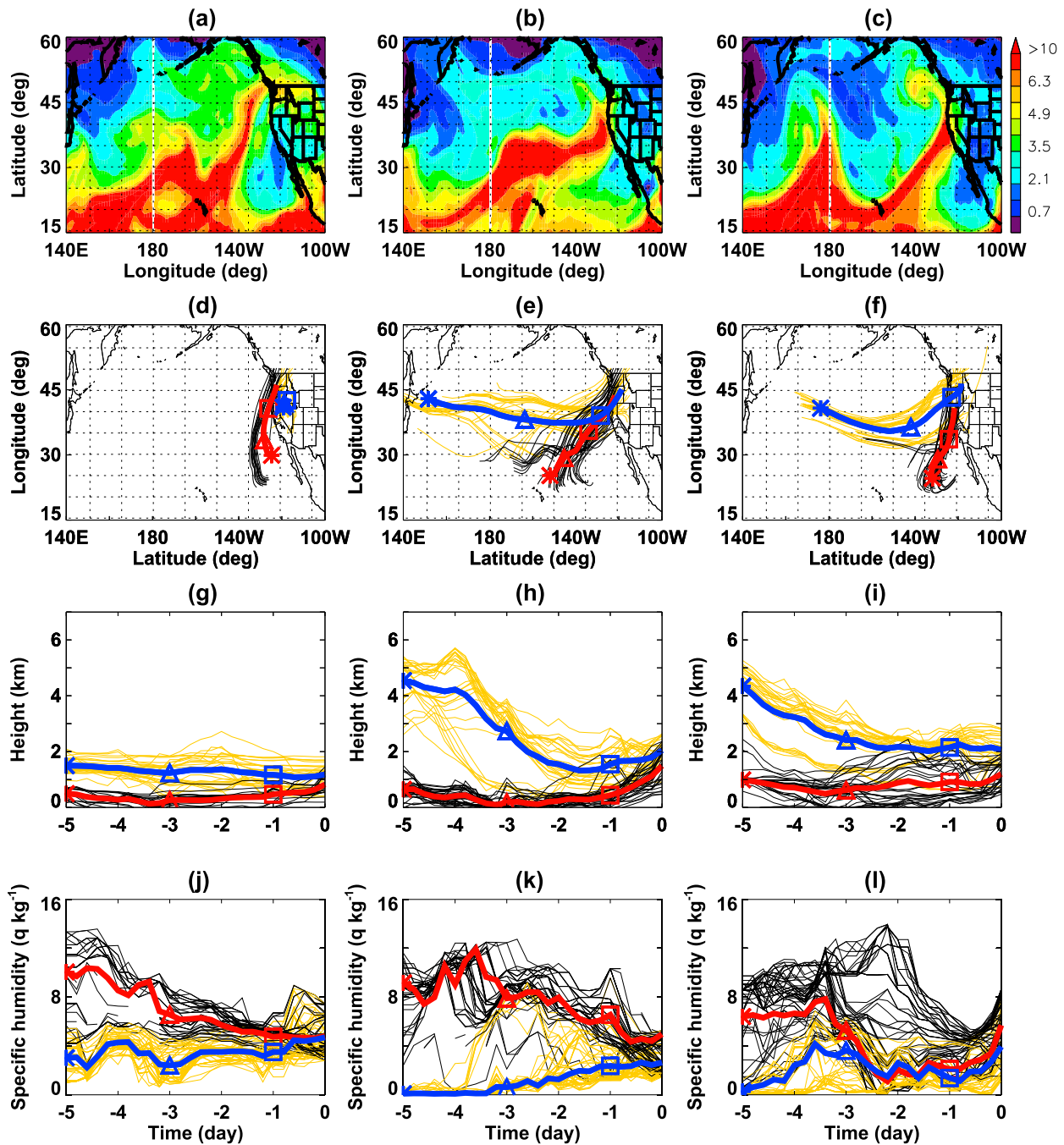
Figure 3. Maps of (a–c) MERRA specific humidity (q) averaged from the surface up to 700 hPa, the (d–f) spatial and (g–i) temporal evolution of 5 day backward trajectories releasing at, and (j–l) water vapor along the trajectories obtained from the nearest location to MERRA q at each grid point for (Figures 3a, 3d, 3g, and 3j) 19 January 2005, (Figures 3b, 3e, 3h, and 3k) 14 January 1998, and (Figures 3c, 3f, 3i, and 3l) 16 February 2004. The symbols (squares, triangles, and stars) represent the positions of the trajectory at the time from days −1, −3, and −5, respectively.

and upward tracks, and gradually gain moisture. As seen in Figure 3, the trajectories at or above 850 hPa are originally dry because they mostly come from higher, extratropical regions, but they may get moisture due to evaporation of precipitation, vertical mixing associated with the instability of the atmosphere, and eddy and advective horizontal transport [*Ryoo et al.*, 2013; *Ploeger et al.*, 2013].

To further quantify the differences in precipitation among the different types of AR events, we calculate the probability density functions (PDFs) of precipitation intensities within the target region. Figures 4a, 4c, and 4e

Table 2. The Means and Standard Deviations (Marked by ±) of the Longitude, Latitude, Pressure, and Specific Humidity (*q*) at Selected Times of the Trajectories During 5 Day Backward Trajectory Simulations for AT-Only, AT + AE, and AT + DE Events

Time	−4 days	−2 days	−1 days	−6 h	0
		AT Only			
		AT (Below 1 km)			
longitude	−135.2 ± 10.4	−131.3 ± 8.4	−126.8 ± 5.5	−122.5 ± 2.4	−121.4 ± 2.0
latitude	31.1 ± 5.0	36.5 ± 3.1	40.2 ± 3.0	43.2 ± 3.1	44.2 ± 3.3
p	938.0 ± 47.7	907.1 ± 57.4	887.5 ± 53.8	842.9 ± 43.7	819.7 ± 46.3
q	5.6 ± 3.5	4.7 ± 3.0	3.9 ± 2.7	3.6 ± 2.1	4.0 ± 2.1
		AT (Above 1 km)			
longitude	−139.8 ± 18.7	−126.3 ± 8.7	−121.3 ± 3.9	−118.9 ± 1.8	−118.4 ± 1.6
lattitude	37.9 ± 6.1	39.6 ± 3.2	41.1 ± 2.1	42.5 ± 2.6	43.0 ± 2.8
p	822.9 ± 58.7	845.4 ± 73.0	839.9 ± 62.4	819.2 ± 44.3	804.8 ± 47.4
q	3.4 ± 2.8	2.4 ± 1.5	2.8 ± 1.6	3.8 ± 2.0	3.8 ± 1.7
		AT + AE			
		AT			
longitude	−143.8 ± 15.7	−133.6 ± 9.6	−127.4 ± 5.7	−121.7 ± 2.2	−120.5 ± 1.7
latitude	33.9 ± 5.0	36.2 ± 4.3	38.6 ± 3.3	42.0 ± 2.5	43.1 ± 2.6
p	874.8 ± 88.0	870.0 ± 87.0	860.1 ± 66.7	808.3 ± 60.7	785.2 ± 61.1
q	4.9 ± 3.5	4.0 ± 3.2	3.4 ± 2.6	3.2 ± 2.3	3.7 ± 2.2
		AE			
longitude	−168.0 ± 26.0	−140.4 ± 14.5	−129.1 ± 8.3	−121.5 ± 3.0	−120.2 ± 2.3
latitude	45.0 ± 7.8	41.0 ± 5.9	40.8 ± 3.3	43.3 ± 2.6	44.4 ± 2.8
p	623.8 ± 141.0	755.3 ± 113.3	787.5 ± 87.8	772.4 ± 74.7	748.7 ± 71.9
q	1.1 ± 1.6	1.6 ± 2.0	2.3 ± 2.1	2.8 ± 2.4	4.0 ± 2.4
		AT + DE			
		AT			
longitude	−140.8 ± 18.3	−132.1 ± 12.5	−125.7 ± 7.6	−121.5 ± 2.9	−120.7 ± 2.6
latitude	32.1 ± 5.2	35.4 ± 4.3	38.4 ± 3.7	41.9 ± 2.4	43.0 ± 2.4
p	845.9 ± 115.3	843.7 ± 109.4	847.5 ± 65.7	800.4 ± 40.3	782.2 ± 45.3
q	5.3 ± 3.8	4.2 ± 3.5	3.8 ± 3.0	3.0 ± 2.3	4.2 ± 2.4
		DE			
longitude	−170.8 ± 29.5	−137.9 ± 15.1	−125.1 ± 7.1	−119.3 ± 2.4	−118.6 ± 1.9
latitude	45.8 ± 7.7	41.9 ± 5.9	41.0 ± 4.5	42.7 ± 4.1	43.0 ± 4.2
p	538.3 ± 133.3	638.8 ± 153.7	698.1 ± 85.6	716.6 ± 75.3	727.7 ± 71.4
q	0.6 ± 1.1	2.5 ± 2.9	2.1 ± 2.2	1.8 ± 1.5	3.3 ± 1.7

show the PDFs of precipitation in the target region, for AR categories as well as the PDFs for each trajectory type. There are statistically significant differences in the mean and the PDFs between all AR events, i.e., the differences between AT only and AT + DE, between AT + AE and AT + DE, and between AT only and AT + AE are significant at or above the 90% confidence level (i.e., p values < 0.01). The Student's t test was used to determine the significance of the difference in the mean, while the *two-sided Kolmogorov-Smirnov test* [*Press et al.*, 1992] was used to determine the significance of the difference of the total precipitation PDFs. We have also quantified the occurrence of extreme precipitation within the AR events. We consider two different critical (threshold) values for extreme precipitation: rain rates that exceed 20 or 30 mm d^{-1}. Specifically, the probability of extreme precipitation (the probability is calculated as the ratio of the number of precipitation cases larger than the given threshold over the number of total precipitation events larger than 0.1 mm d^{-1} within the target region) is highest for AT trajectories and lowest for DE trajectories (Figures 4b, 4d, and 4f). There are different contributions of each trajectory type to precipitation. For example, AT and AE trajectories are similarly associated with high precipitation for AT + AE (Figures 4c and 4d) while AT trajectories are much more strongly associated with high precipitation than DE for AT + DE (Figures 4e and 4f). The results are insensitive to the threshold used to define "extreme" (e.g., the probabilities for precipitation larger than 20 and 30 mm d^{-1} are all highest for AT trajectories). Hence, these calculations confirm the above conclusion that the trajectory types where parcels ascend (AT, AE) are mainly responsible for heavy precipitation while descending or parallel trajectories (DE) are not typically associated with heavy precipitation.
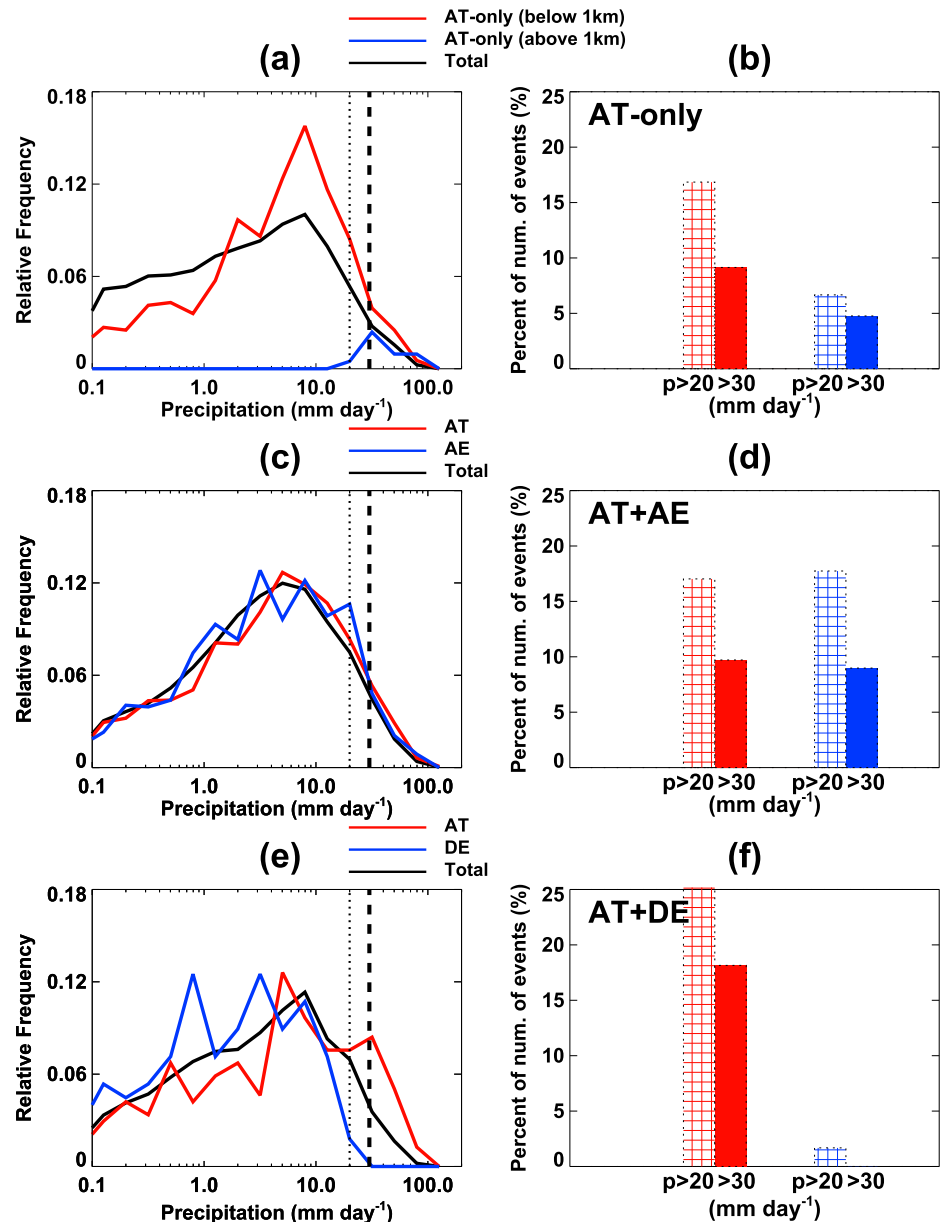
Figure 4. (a, c, and e) Probability density functions (PDFs) of precipitation corresponding to the mean trajectories and (b, d, and f) percentages of number of events when precipitation is larger than 20 (gridded fill), and 30 (solid fill) mm d^{-1} for AT-only (red), AE (blue), and DE (blue) trajectories. The red (blue) lines represent the PDF of precipitation for mean trajectories of AT (AT above 1 km for AT only), AE, and DE), respectively. The black lines in PDFs are the total PDFs in both types. The vertical (dotted, thick dashed) lines in Figures 4a, 4c, and 4e indicate precipitation intensity of 20 and 30 mm d^{-1}.

3.4. Meteorological Fields and Transport Process
3.4.1. Characteristics of Meteorological Fields

The meteorological fields also show different characteristics among AT-only, AT + AE, and AT + DE events. Figure 5 shows that the composite mean sea level pressure, temperature, zonal, meridional, and vertical wind averaged over 700–1000 hPa corresponding to AT-only, AT + AE, and AT + DE events. The zonal wind for AT only is stronger in tropical regions (~35°N and below) and in the northwestern coast compared to that for AT + AE and AT + DE. Among the types in Figure 5, the temperature for AT-only trajectories is higher than that for AT + AE, ranging from 1 K (inland) to 4 K (coastal region). This is reasonable because AT trajectories come from the warmer tropics (Figures 5a, 5c, and 5e). For all events, the minimum sea level pressure (less than 990 hPa) from the northern Pacific basin penetrates further southward. A single low-pressure center is
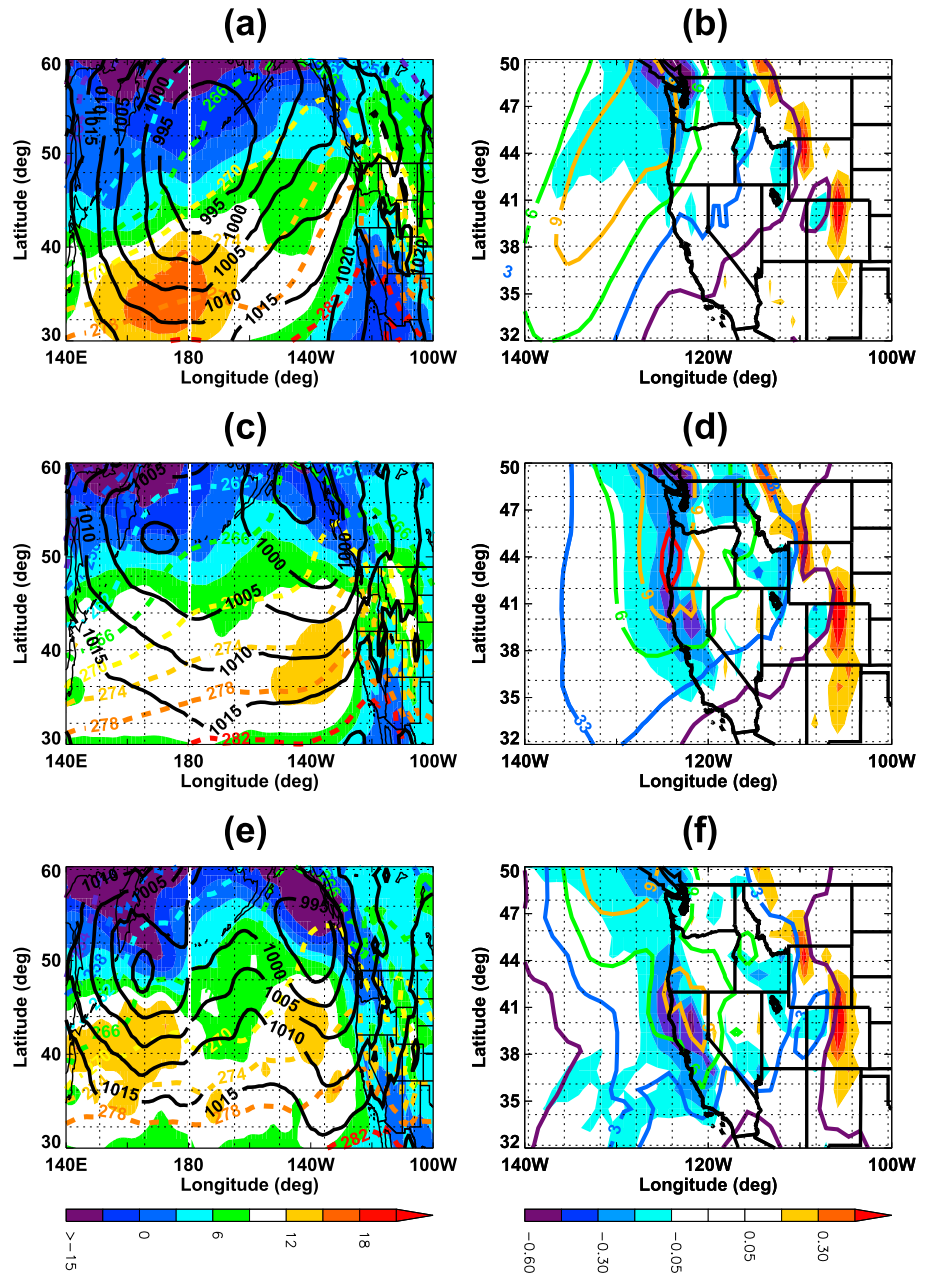
Figure 5. Composite mean (a, c, and e) sea level pressure (black solid line, unit in hPa), zonal velocity (shading, unit in m s^{-1}), overlaid by temperature (dashed line, unit in K), and (b, d, and f) composite mean vertical velocity (ω, unit in Pa s^{-1}, shading, negative value means upward motion) overlaid by meridional velocity (contour), averaged over 700–1000 hPa for (Figures 5a and 5b) AT-only, (Figures 5c and 5d) AT + AE, and (Figures 5e and 5f) AT + DE events.

located further north along the U.S. West Coast, associated with a maximum in meriodional wind for AT only, while double low-pressure centers are located in the further northern Pacific, making a strong trough-ridge structure for AT + AE and AT + DE. These low-pressure systems during the winter in NH are consistent with the finding by *Lackmann and Gyakum* [1999] and *Neiman et al.* [2008]. The upward vertical velocity of AT only (in Figure 5b) is located further north of the West Coast of the U.S. with a strong meridional wind collocated, and this vertical motion is slightly stronger by ~ −0.2 Pa s^{-1} than that of AT + AE and AT + DE especially over the coastal regions of Oregon and Washington (Figures 5b and 5d). The vertical velocity of AT + AE is stronger than that of AT + DE by −0.1 to −0.3 Pa s^{-1}, especially over the northwestern U.S. (Figures 5d and 5f). It is also worth noting that the distributions of ascent (Figures 5b, 5d, and 5f) match the precipitation

fields (Figures 2c, 2f, and 2i). For example, heavy precipitation mostly distributes over the northwest of the U.S. for AT only; the broad regions of the whole West Coast of the U.S. for AT + AE; and the southwestern U.S. including northern California for AT + DE. Another interesting question is raised by these results: what physical processes control the location of these strong ascent and descent motions during AR events over the western U.S.? We explore this more in detail in the following section.

3.4.2. PV Intrusions

Figures 1, 2e, and 2h showed that a large portion of trajectories of extratropical origin (AE and DE trajectories) come from the high altitudes (400–600 hPa). The PDFs in Figure 4 also show that the precipitation location and intensity appear to be related to the trajectory types having different origins, suggesting that the variability in cold season precipitation over the western U.S. can be closely linked to the upper level disturbances.

One major cause of the upper level disturbances is Rossby wave propagation and its breaking, which can lead to "intrusions" of air having high PV into the tropical and subtropical upper troposphere [*Waugh and Funastu*, 2003; *Waugh*, 2005]. Recent studies showed that these PV intrusions (Rossby wave breakings) are a major cause of the variability of subtropical RH, surface cyclone, and precipitation timing [*Ryoo et al.*, 2008; *Moore et al.*, 2010]. Here we show how upper level PV intrusions are linked to the RH, and eventually cold season precipitation during AR events over the western U.S.

A key feature in Figure 6 is that the q in the lower level is closely tied to the upper level PV (Figures 6a, 6ac, and 6ae). A plume of large tropospheric q and southwesterly flow (averaged over 850–700 hPa) to the West Coast of the U.S. are associated with the directions and locations of the upper level PV, and the extreme moisture transport into the West Coast of the U.S. usually occurs ahead of these upper level PV (Figures 6a, 6ac, and 6ae). A region of PV greater than 3 potential vorticity unit (PVU) was located near the center of the cyclone (e.g., the low geopotential heights and low sea level pressure centers (not shown)), indicating that flow associated with the upper level PV was partly responsible for the northward warm sector moisture transport during the AR event. In addition, what happens commonly to all types is that the highest RH averaged over surface to 250 hPa is observed ahead (on the west side) of high composite mean PV for all categories. These locations of vertically averaged high/low RH are also related to the strong/weak ascent in each category, especially over the coastal regions (37°N–50°N) (see Figures 5, 6b, 6d, and 6f). While it appears that upper level PV is associated with moisture transport, a circular region of larger lower level tropospheric PV (0.5–1 PVU) is also observed along with the high q elongated from the tropics (not shown), implying not only upper level PV but also the lower tropospheric PV develops together and "supports" the northward and poleward moisture transports.

Massacand et al. [2001] shows that the cloud diabatic heating associated with the upstream cyclogenesis strengthens downstream negative upper level PV anomalies, and the flow associated with these anomalies subsequently helps existing positive PV anomalies to transform into an elongated PV streamer. Their study prompts us to examine the influence of diabatic heating on the upper level PV development among different AR categories. Figure 7 shows that the strong upward motions usually occur in the west of negative upper level PV anomalies (low PV) and the east of positive upper level PV anomalies (high PV) while the downward and the weakened upward motions are induced to the east of large negative upper level PV anomalies (around 300–400 hPa, 120–110°W, Figures 7e and 7f) especially for AT + DE. The stronger cyclonic (positive) PV anomalies associated with the positive diabatic heating anomalies appear to enhance the vertical ascent over the Pacific Ocean around 145°W–125°W (130°W–120°W, 135°W–125°W) for AT-only (AT + AE, AT + DE) AR events at day − 1, and they subsequently move eastward to the West Coast of the U.S. (120°W) at day 0. Below the regions of enhanced diabatic heating, there are regions of strong diabatic cooling (up to −6 K d^{-1}). Figure 7 demonstrates that the diabatic heating anomalies produce the lower cyclonic (positive) PV maximum, and above the midlevel maximum of the heating, finally modify the anticyclonic (negative) PV anomalies in response differently for each AR category.

The features shown in Figure 7 are consistent with the results of *Wernli and Davies* [1997] and *Massacand et al.* [2001], which revealed the impact of a midlevel diabatic heating maximum on promoting negative upper level PV anomalies during cyclogenesis events. From their interpretation and our results shown in Figure 7, we can speculate that the diabatic heating influences the PV developments, and the influence also varies with the size and shape of the cyclones developed among the AR types. The general validity of this inference,
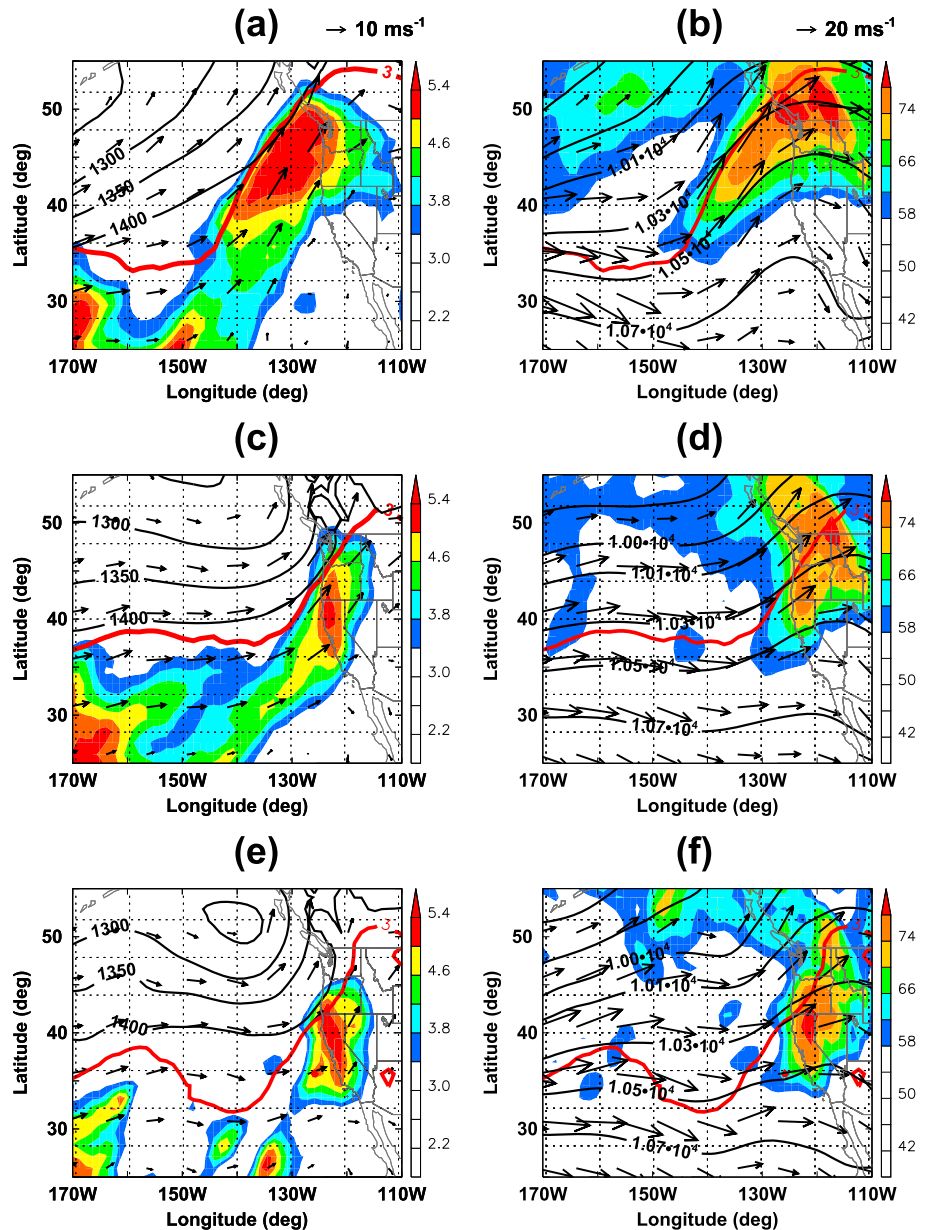
Figure 6. (a, c, and e) Composite mean of 850 hPa horizontal wind (vectors), 850 hPa geopotential heights (black solid lines), and specific humidity (q) (g kg^{-1}) averaged over 850–700 hPa, and (b, d, and f) composite mean of 250 hPa horizontal wind (vectors), 250 hPa geopotential heights (black solid lines), and RH (shading) averaged from the surface to 200 hPa for (Figures 6a and 6b) AT-only, (Figures 6c and 6d) AT + AE, and (Figures 6e and 6f) AT + DE events. PV of 3 PVU (red lines, 1 PVU = 10^{-6} km^2 kg^{-1} s^{-1}) is superimposed upon all panels.

however, remains to be examined by further individual case studies. In addition, what makes this strong diabatic heating is beyond the scope of this study, but the release of the latent heat due to the formation of clouds during ascent may be one of the dominant factors as shown by [*Joos and Wernli*, 2012].

The composite RH anomalies shown in Figure 8 demonstrate that there are clear relationships between upper level PV anomalies and RH: high (low) RH anomalies are collocated with the negative (positive) upper level PV anomalies, and they are vertically coherent throughout the whole altitude range from below 400 hPa, to around 200 hPa for all AR categories. Here these high/low distinctions refer to the longitudinal variations of RH in the east/west. Over the southwestern U.S. and California (32°N–42°N), the vertical separation of high/low RH anomalies occurs around 140°W (130°W, 125°W), with strong vertical coherence of high/low RH
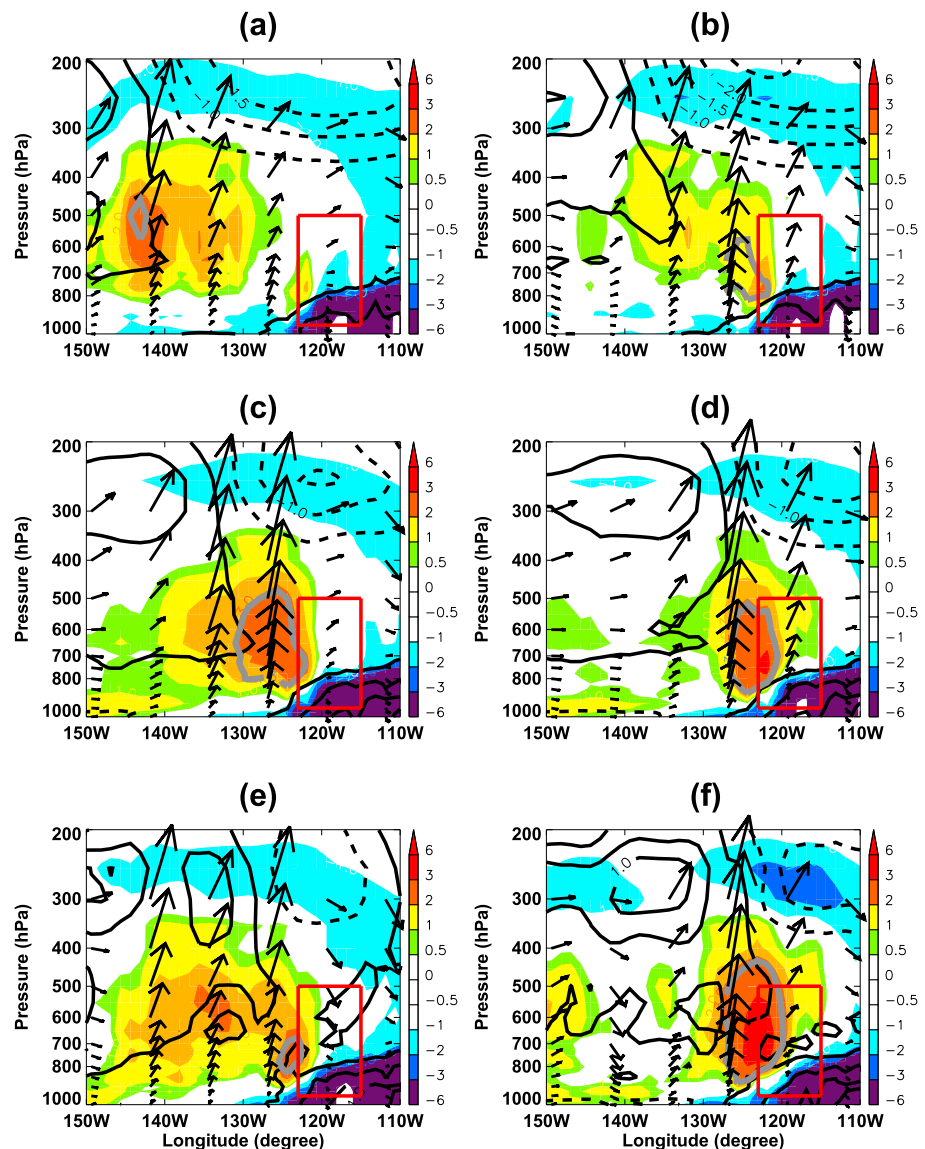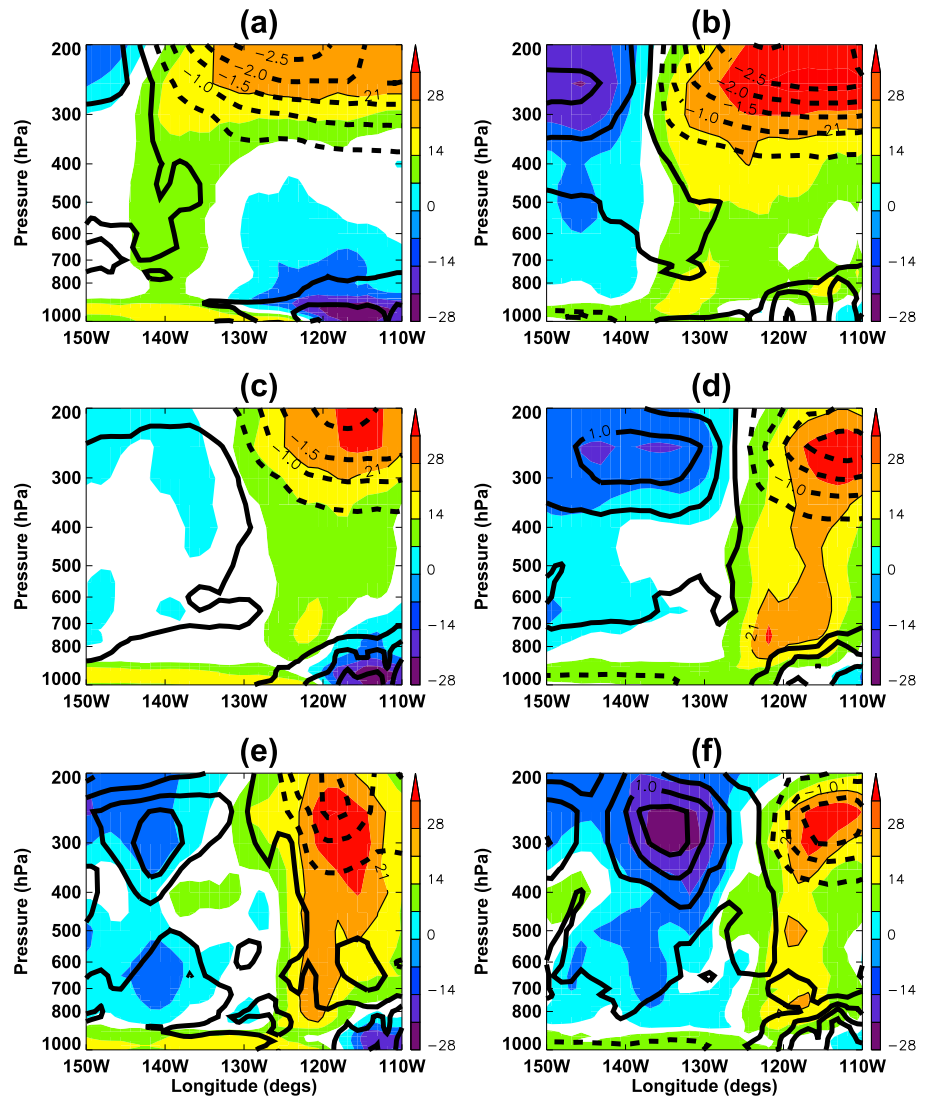
Figure 7. Longitude-height cross sections of composites total diabatic heating anomalies (shading, unit in K day^{-1}), and potential vorticity anomalies (PV, thick line, unit in PVU) from the zonal mean, and wind vectors averaged over the target latitude (34–50°N) for (a, b) AT-only, (c, d) AT + AE, and (e, f) AT + DE events at (Figures 7a, 7c, and 7e) day − 1, (Figures 7b, 7d, and 7f) day 0 (from the date of individual AR event). The arrows represent wind vectors. The red boxes represent the heights at 500–800 hPa, indicating where trajectories behave vertically. The vertical velocity [m s^{-1}] is converted from ω [Pa s^{-1}] and multiplied by scaling factor (10^5). The solid (dashed) lines represent the positive (negative) PV anomalies with 0.5 PVU interval.

anomalies over the West Coast of the U.S. for AT only (AT + AE, AT + DE) (Figures 8a, 8c, and 8e). The stronger cyclonic (positive) PV anomalies associated with diabatic heating appear to increase RH by enhancing the ascent over the southwestern U.S., especially for AT + DE (Figures 7e, 7f, and 8e). Over the northwestern U.S. including Oregon and Washington (42°N–50°N), however, the vertical coherence of high RH anomalies gets much stronger especially for AT + AE, and this appears to be due to stronger cyclonic PV anomalies which promote stronger vertical motion over the northwestern U.S. around 125°W.

While Figures 7 and 8 demonstrate that there are strong relationships among upper level PV, RH, and vertical motions, these do not directly indicate whether precipitation is also affected by the location and shape of PV. We performed a regression analysis and obtained high correlations when we regress between RH at 250 hPa of the West Coast of the U.S. and PV to the west by $10 − 20°$ from the given longitude for all AR events (e.g., 0.86, 0.78, and 0.80 between upper level PV at 250 hPa and RH at 250 hPa over the western U.S. for AT only, AT + AE,

Figure 8. Longitude-height cross sections of composite RH anomalies from the zonal mean (shading) overlaid by composite upper level PV anomalies from the zonal mean averaged over (a, c, and e) southwestern U.S. and California (32–42°N) and (b, d, and f) northwestern U.S. (42–50°N) for (Figures 8a and 8b) AT-only, (Figures 8c and 8d) AT + AE, and (Figures 8e and 8f) AT + DE events. The solid (dashed) lines represent the positive (negative) PV anomalies with 0.5 PVU interval.

and AT + DE), respectively. The correlation coefficients are particularly high over the northwestern U.S. A similar feature is found for the correlation between upper level PV and precipitation, although the correlation is smaller (0.4–0.7) than those between upper level PV and RH. Overall, these high correlations indicate that the regional difference of the western U.S. precipitation is linked to the location, shapes, and timing of the upper level PV aloft (not shown).

In regions where there are few PV intrusion events, for example, the regions over 25°N–45°N, 100°W–80°W, the correlation obtained by regression both between upper level PV and precipitation and the upper level PV and RH is very low (<0.1), indicating that precipitation fluctuations are not closely linked with PV fluctuations in these regions (not shown).

3.4.3. PV Orientations

The different locations and intensities of upper level PV anomalies from Figures 7 and 8 hint that there is a different tendency of trajectory categories in the orientation of the PV intrusions. *Ryoo et al.* [2013] shows that during NH winter, precipitation is closely related to the locations and types (different phases) of PV intrusions, such as anticyclonic (LC1-like) and cyclonic (LC2-like) Rossby wave breaking (RWB). To further explore how the
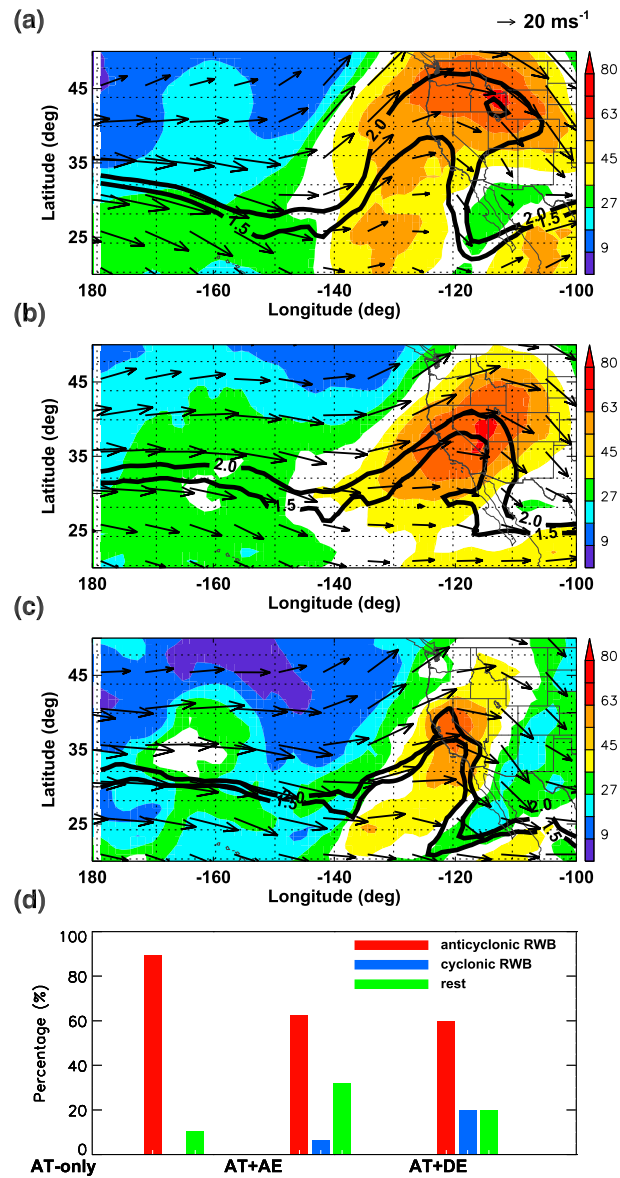
Figure 9. A map of MERRA RH (shading) and horizontal wind (vector) at 200–250 hPa for anticyclonic Rossby wave breaking (RWB) events for (a) AT-only, (b) AT + AE, and (c) AT + DE events. (d) The percentages of the PV orientation for each AR events. The three categories are used: anticyclonic RWB (LC1-like, red), cyclonic RWB (LC2-like, blue), and the unclear rest (green). The percentage is relative to the total number of AR events used in this study. PV averaged over 200–250 hPa are overlaid (1.5 and 2.0 PVU).

orientation of PV intrusions affects the AR types and precipitation patterns, we divided PV intrusions events into two different RWB types depending on their orientation relative to their maximum values. Here we identify this in a slightly different but similar manner to *Waugh* [2005] and *Ryoo et al.* [2013]: All days where PV ≥ 2.5 PVU at 20°N–50°N within 10° of longitude from the eastern Pacific and the West Coast of the U.S. region (160°W–110°W) were identified. If the orientation from the PV maximum is northeast-southwestward, then it is called an anticyclonic Rossby wave breaking (LC1-like) event, and if the orientation from the PV maximum is northwest-southeastward, then it is called a cyclonic Rossby wave breaking (LC2-like) event. An occurrence on a given day is counted as a single event. In this way, we classified PV intrusions during all AR events used in this study into three types: anticyclonic, cyclonic, and unclear rest. For AR events having a complicated PV curvature or rapidly evolving PV forms, which are difficult to classify as either anticyclonic or cyclonic RWB, then we refer them as the "unclear rest." A similar separation was reported by *Martius et al.* [2006], which divided PV intrusions (they referred to them as PV streamers) into four categories, LC1 (anticyclonic), meridional, LC2 (cyclonic), and the rest. They also showed that there is a slight preference of the streamer orientation on regional precipitation and LC1 and meridional are associated with similar cyclogenetic structures.

The results are summarized in Figure 9. Notably, most of the AR events for all AR types show preference to anticyclonic RWB events although the shapes of composite PV associated with anticyclonic RWB events are different: for AT only, the shapes of PV make a sharper turn around 140°W–130°W northward than for AT + AE and AT + DE (Figures 9a–9c). The shapes of PV of AT + AE and AT + DE are similar, but those of AT + AE (AT + DE) are less (more) trapped between PV contours over the broad western (southwestern) U.S. as anticyclonic RWB develop over the West Coast of the U.S (Figures 9b and 9c). Overall, anticyclonic RWB types (79 events) are much more dominant types than the cyclonic RWB types (eight events) during all AR events (about 10 times more frequent). Ninety percent of AT-only AR events show a preference of anticyclonic RWB-type orientation, but none of AT-only AR events has cyclonic RWB-type orientation. Both AT + AE and AT + DE have similar preference of anticyclonic RWB-type orientation with a slightly larger tendency toward cyclonic RWB and unclear type for AT + DE. The results shown in Figure 9 is consistent with recent studies, showing that strong
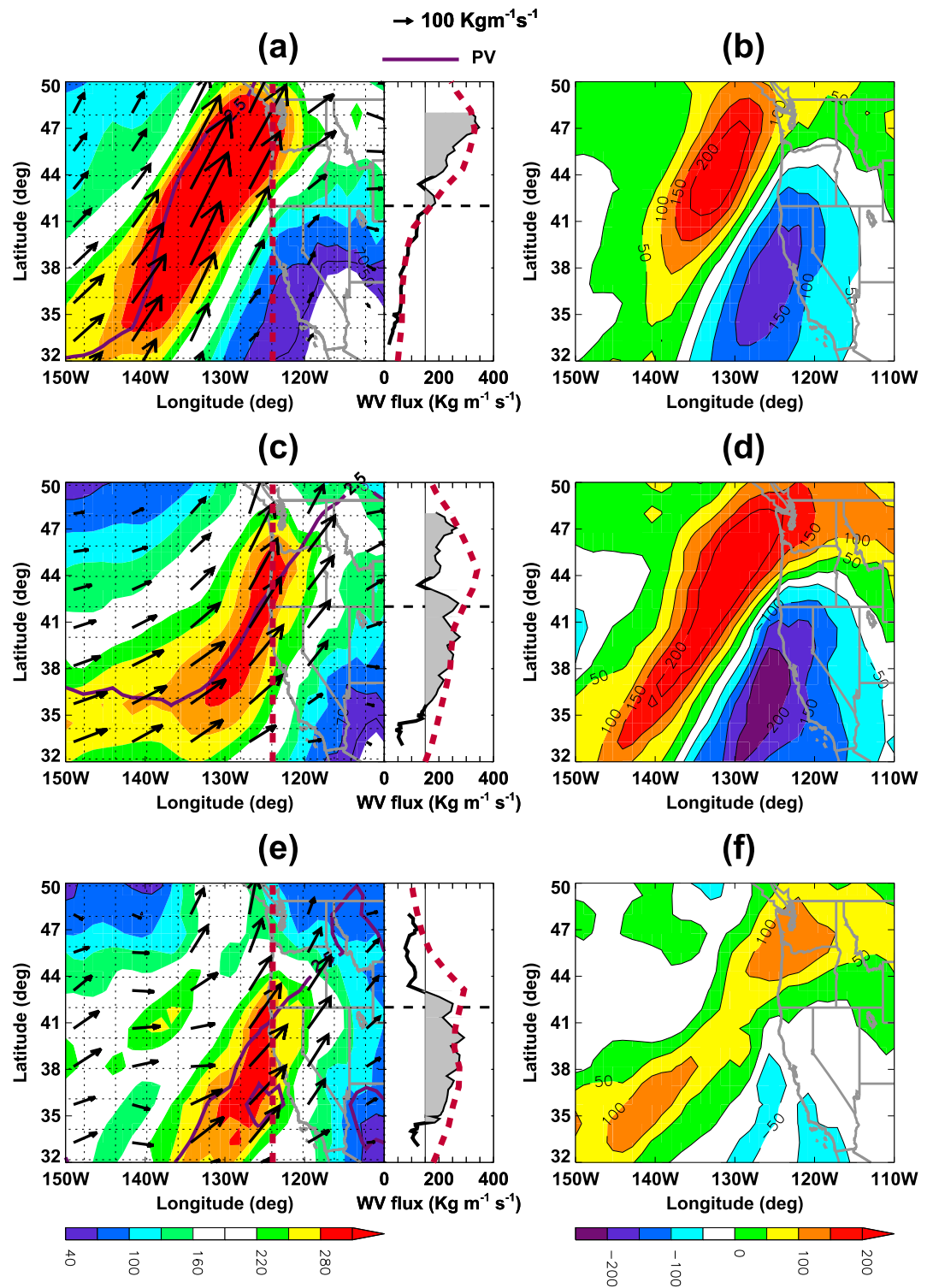
Figure 10. (a, c, and e) The composite mean vertically integrated horizontal water vapor fluxes (color and arrows, unit in kg m^{-1} s^{-1}) overlaid by PV (2.5 PVU) (left) and the components orthogonal to the coastline (right) for (Figures 10a and 10b) AT-only, (Figures 10c and 10d) AT + AE, and (Figures 10e and 10f) AT + DE events. Vector represents the magnitude of water vapor fluxes (unit in kg m^{-1} s^{-1}). The brown dashed lines in Figures 10a, 10c, and 10e represent the water vapor fluxes crossing the coastal region (124°W). The horizontal dashed lines indicate latitude 42°N, and vertical solid line indicates 150 kg m^{-1} s^{-1} in Figures 10a, 10c, and 10e. (b, d, and f) The difference map of the water vapor fluxes between AT only and AT + AE, between AT only and AT + DE, and between AT + AE and AT + DE, respectively.

landfalling ARs are closely related to the development of anticyclonic RWB events in the northeastern Pacific and the West Coast of North America [*Payne and Magnusdottir*, 2014].

3.4.4. Vertically Integrated Water Vapor Fluxes

To examine the vapor transport associated with the different types of AR events, we compute vertically integrated water vapor fluxes corresponding to AT-only, AT + AE, and AT + DE events in Figure 10. The vertically integrated water vapor fluxes are calculated as $1/g \int_{p_0}^{p_1} \overline{qU} dp$, where $\overline{qU}$ denotes the mean values of qU within each adjacent pressure layer (dp), q is the specific humidity, $U = (u, v)$ is the horizontal wind component, g is the gravitational constant, $p_0 = 1000$ hPa, and $p_1 = 150$ hPa. As shown in Figure 10, the water vapor fluxes are associated with the shape of composite mean upper level PV. They are large over the northwestern U.S. including Oregon and Washington for AT only, over the whole range of the West Coast of the U.S. for AT + AE, and over the southwestern U.S. including California for AT + DE (Figures 10a, 10c, and 10e). In order to see the impact of AR on the coastal regions, we also calculate the component of water vapor fluxes orthogonal to the coastline as the inner product between the normal vector to the coastline (33°N–48°N) and the wind vector along the coastline. The coastline data are available at NOAA National Geographic Data Center (http://www.ngdc.noaa.gov/mgg/coast/). The wind data at the coastline are obtained by the method of bilinear interpolation. Normal to the coastline in Oregon and Washington, the AT-only (AT + DE) composite has the largest (smallest) water vapor flux ranging over 150–350 (70–110) kg m^{-1} s^{-1}, (see Figures 10a (right) and 10e (right)). The water vapor fluxes for AT only (0–400 kg m^{-1} s^{-1}) are larger by 0–50 kg m^{-1} s^{-1} over Washington and British Columbia, but smaller by 0–150 kg m^{-1} s^{-1} over northern California (around 42°N) than those for AT + AE and AT + DE (Figures 10b and 10d). The water vapor fluxes for AT + AE is larger over the northwestern U.S. than for AT + DE, and smaller over the southwestern U.S. including north California (less than 50 kg m^{-1} s^{-1}, Figure 10f). Figure 10 distinctly demonstrates that the vertically integrated water vapor fluxes are large in the northwestern U.S. (ranging from 42°N to 50°N) for AT only and in the California or Nevada (ranging from 34°N to 42°N) for AT + AE and AT + DE, and these are all closely related to the direction of horizontal winds, and the shape of composite mean upper level PV.

Total precipitable water (defined as $1/g \int_{p_0}^{p_1} \overline{q} dP$) also shows similar patterns to the water vapor fluxes between AT only, AT + AE, and AT + DE. However, the difference of precipitable water among AR types is too small to explain the difference of water vapor flux or precipitation (not shown). This emphasizes that strong winds associated with wintertime tropical and extratropical storms that undergo ascent near the target regions (Figures 5 and 6), along with high precipitable water, are necessary to reinforce stronger moisture transport that leads to higher precipitation.

4. Conclusions

We have characterized the relationship between water vapor transport pathways, characteristics of synoptic-scale meteorological conditions, and extreme precipitation of the West Coast of the U.S. during AR events from December to March in 1997–2010 using a back trajectory model. *K*-means cluster analysis shows that the trajectories during AR events can be classified into three types, and two of them are closely associated with AR events: the two of them associated with AR events are (i) trajectories with ascending motion near the West Coast of the U.S. and tropical origins (ascending tropical; AT) and (ii) trajectories with similar ascending motion but extratropical origins (ascending extratropical; AE). The third type, which accompanies but is not directly associated with AR events, consists of trajectories with extratropical origin but descending or horizontal motion near the West Coast of the U.S. (descending or nearly horizontal extratropical; DE). We found that the majority of AR events are characterized by a combination of two of these trajectory types with around 76% by AT and AE trajectories (AT + AE), 16% by AT-only trajectories (AT), and around 8% characterized by AT + DE trajectories.

The intensity and location of precipitation vary among the different AR events. The PDF analysis shows that the chance of precipitation larger than 20 (30) mm d^{-1} is 14.7 (8.7)% for AR events in AT + AE, 12.7 (9.4)% for AT only, and 16.6 (9.1)% AT + DE over a broad U.S. West Coast target area. The AT-only AR events are accompanied by steeper northward winds that impinge on the mountainous coastal region of the northwestern North America such as Oregon, Washington, and British Columbia. The AT + AE AR events are most frequent, and both AT and AE trajectories are associated with the northward and eastward wind along the West Coast of the U.S. that enhances moisture transport into northern California and Oregon, leading to higher precipitation

there. The AT + DE events are relatively rare, but AT trajectories of the AT + DE AR events play a major role in cross-coast water vapor transport through the extratropical cyclones, resulting in intense precipitation over the southwestern U.S.

Distinctive meteorological conditions are found among the different AR trajectory types. The different patterns of upward motions among AR events are related to the strong diabatic heating/cooling regions, and these regions are also closely tied to PV anomalies. Furthermore, there is a consistent RH structure for composite upper level PV anomalies in all AR trajectory types, with high (low) RH anomalies collocated with the strong (weak) upward motion and negative (positive) PV anomalies, which are on the west (east) of low PV. The regions of high/low RH are also vertically coherent throughout the altitude range, but their magnitudes differ depending on the strength of vertical ascent and the shape of PV for given AR category. In addition, about 66% (79 events out of 120 events studied here) of the AR events are associated with the anticyclonic RWB. Clear distinction in the vertically integrated water vapor fluxes also supports the relative difference in location and intensity of precipitation. The water vapor fluxes are large in AT-only (AT + AE, AT + DE) events in the northwestern U.S. (broad regions of the U.S., southwestern U.S.), which tend to produce larger precipitation over there.

This study highlights that the different patterns of trajectory types among AR events are tightly linked to different meteorological conditions, composite mean upper level PV and its anomalies, the water vapor fluxes, and eventually regional difference of precipitation over the West Coast of the U.S. It will be interesting to further explore how the occurrence of AR events of a particular type is linked to antecedent synoptic conditions, modes of large-scale climate variability [*Guan et al.*, 2013], and climate change [*Dettinger*, 2011; *Lavers et al.*, 2013]. According to recent studies, direct poleward transport of tropical moisture within an enhanced IWV band in the eastern Pacific is most likely during the neutral El Niño Southern Oscillation (ENSO) phase [*Bao et al.*, 2006] but least likely during the warm phase [*Matthew and Kiladis*, 1999]. *Dettinger et al.* [2011] showed no reliable correlation between ENSO and pineapple express contributions in central and northern California, but the warming of the Pacific warm pool since 1970s may contribute to the broad declines in the pineapple express type of AR events from the 1980s to 2008. Using five state of the art global climate models in the fifth Climate Model Intercomparison Project, *Lavers et al.* [2013] reported that ARs over the North Atlantic regions will be stronger and more frequent. Continuous efforts to investigate the interannual variability in extreme precipitation such as ARs and their response to climate change will be essential to protect water resources and prevent floods in the western U.S.

References

Appenzeller, C., and H. C. Davies (1992), Structure of stratospheric intrusions into the troposphere, *Nature*, *358*, 570–572.

Bao, J.-W., S. A. Michelson, P. J. Neiman, F. M. Ralph, and J. M. Wilczak (2006), Interpretation of enhanced integrated water vapor bands associated with extratropical cyclones: Their formation and connection to tropical moisture, *Mon. Weather Rev.*, *134*, 1063–1080.

Bosilovich, M., J. Chen, F. R. Robertson, and R. F. Adler (2008), Evaluation of global precipitation in reanalysis, *J. Appl. Meteorol. Climatol.*, *47*, 2279–2299.

Bosilovich, M. G., F. R. Robertson, and J. Chen (2011), Global Energy and Water Budgets in MERRA, *J. Clim.*, *24*, 5721–5739, doi:10.1175/2011JCLI4175.1.

Browning, K. A. (1986), Conceptual models of precipitation systems, *Weather Forecasting*, *1*, 23–41.

Cape, J., N. J. Methven, and L. E. Hudson (2000), The use of trajectory cluster analysis to interpret trace gas measurements at Mace Head, Ireland, *Atmos. Environ.*, *34*, 3651–3663.

Couhert, A., T. Schneider, J. Li, D. E. Waliser, and A. M. Tompkins (2010), The maintenance of the relative humidity of the subtropical free troposphere, *J. Clim.*, *23*, 390–403, doi:10.1175/2009JCLI2952.1.

Dettinger, M. (2011), Climate change, atmospheric rivers, and floods in California—A multimodel analysis of storm frequency and magnitude changes, *J. Am. Water Resour. Assoc.*, *47*(3), 514–523, doi:10.1111/j.1752-1688.2011.00546.x.

Dettinger, M., F. M. Ralph, T. Das, P. J. Neiman, and D. R. Cayan (2011), Atmospheric rivers, floods, and the water resources of California, *Water*, *3*, 445–478, doi:10.3390/w3020445.

Dorling, S. R., T. D. Davies, and C. E. Pierce (1992), Cluster analysis: A technique for estimating the synoptic meteorological controls on air and precipitation chemistry—Method and applications, *Atmos. Environ.*, *26A*, 2575–2581.

Eckhardt, S., et al. (2004), A 15-year climatology of warm conveyor belts, *J. Clim.*, *17*, 218–237.

Fernau, M. E., and P. J. Samson (1990), Use of cluster analysis to define periods of similar meteorology and precipitation chemistry in eastern North America. Part I: Transport patterns, *J. Appl. Meteorol.*, *29*, 735–761.

Funatsu, B. M., and D. W. Waugh (2008), Connections between potential vorticity intrusions and convection in the Eastern Tropical Pacific, *J. Atmos. Sci.*, *65*, 987–1002.

Grubišić, V., R. Vellore, and A. Huggins (2005), Quantitative precipitation forecasting of wintertime storms in the Sierra Nevada: Sensitivity to the microphysical parameterization and horizontal resolution, *Mon. Weather Rev.*, *133*, 2834–2859.

Guan, B., N. P. Molotch, D. E. Waliser, E. J. Fetzer, and P. J. Neiman (2013), The 2010/2011 snow season in California's Sierra Nevada: Role of atmospheric rivers and modes of large-scale variability, *Water Resour. Res.*, *49*, 6731–6743, doi:10.1002/wrcr.20537.

Higgins, R. W., J.-K. E. Schemm, W. Shi, and A. Leetmaa (2000), Extreme precipitation events in the western United States related to tropical forcing, *J. Clim.*, *13*, 793–820.

Huang, L., R. Fu, J. H. Jiang, J. S. Wright, and M. Luo (2012), Geographic and seasonal distributions of CO transport pathways and their roles in determining CO centers in the upper troposphere, *Atmos. Chem. Phys.*, *12*, 4683–4698.

Jain, S., M. Hoerling, and J. Escheid (2005), Decreasing reliability and increasing synchroneity of western North American streamflow, *J. Clim.*, *18*, 613–618.

Joos, H., and H. Wernli (2012), Influence of microphysical processes on the potential vorticity development in a warm conveyor belt: A case-study with the limited-area model COSMO, *Q. J. R. Meteorol. Soc.*, *138*(663), 407–418.

Kalnay, E., et al. (1996), The NCEP/NCAR 40-year reanalysis project, *Bull. Am. Meteorol. Soc.*, *77*(3), 437–471.

Kerr, R. A. (2006), Rivers in the sky are flooding the world with tropical waters, *Science*, *313*(5786), 435, doi:10.1126/science.313.5786.435.

Knippertz, P., and J. E. Martin (2007), A Pacific moisture conveyor belt and its relationship to a significant precipitation event in the Semiarid Southwestern United States, *Weather Forecasting*, *22*, 125–144, doi:10.1175/WAF963.1.

Knippertz, P., and H. Wernli (2010), A Lagrangian climatology of tropical moisture exports to the northern hemispheric extratropics, *J. Clim.*, *23*, 987–1003.

Lackmann, G. M. (2002), Cold-frontal potential vorticity maxima, the low-level jet, and moisture transport in extratropical cyclones, *Mon. Weather Rev.*, *130*, 59–74.

Lackmann, G. M., and J. R. Gyakum (1999), Heavy cold-season precipitation in the Northwestern United States: Synoptic climatology and an analysis of the flood of 17–18 January 1986, *Weather Forecasting*, *14*, 687–700.

Lavers, A. D., R. P. Allan, G. Villarini, B. Lloyd-Hughes, D. J. Brayshaw, and A. J. Wade (2013), Future changes in atmospheric rivers and their implications for winter flooding in Britain, *Environ. Res. Lett.*, *8*(3), 034010, doi:10.1088/1748-9326/8/3/034010.

Madonna, E., H. Wernli, H. Joos, and O. Martius (2014), Warm conveyor belts in the ERA Interim data set (1979–2010). Part I: Climatology and potential vorticity evolution, *J. Clim.*, *27*, 3–26.

Martínez-Alvarado, O., H. Joos, J. Chagnon, M. Boettcher, S. L. Gray, R. S. Plant, J. Methven, and H. Wernli (2014), The dichotomous structure of the warm conveyor belt, *Q. J. R. Meteorol. Soc.*, *140*, 1809–1824, doi:10.1002/qj.2276.

Martius, O., E. Zenklusen, C. Schwierz, and H. C. Davies (2006), Episodes of alpine heavy precipitation with an overlying elongated stratospheric intrusion: A climatology, *Int. J. Climatol.*, *26*, 1149–1164.

Massacand, A. C., H. Wernli, and H. C. Davies (1998), Heavy precipitation on the Alpine southside: An upper level precursor, *Geophys. Res. Lett.*, *25*, 1435–1438, doi:10.1029/98GL50869.

Massacand, A. C., H. Wernli, and H. C. Davies (2001), Influence of upstream diabatic heating upon an Alpine event of heavy precipitation, *Mon. Weather Rev.*, *129*, 2822–2828.

Matthew, A. J., and G. N. Kiladis (1999), Interactions between ENSO, transient circulation, and tropical convection over the Pacific, *J. Clim.*, *12*, 3062–3086.

Moncrieff, M. W., M. A. Shapiro, J. M. Slingo, and F. Molteni (2007), Collaborative research at the intersection of weather and climate, *World Meteorol. Organ. Bull.*, *56*(3), 204–211.

Moore, R. W., O. Martius, and T. Spengler (2010), The Modulation of the subtropical and extratropical atmosphere in the Pacific basin in response to the Madden–Julian Oscillation, *Mon. Weather Rev.*, *138*, 2761–2779.

Neiman, P. J., F. M. Ralph, G. A. Wick, J. D. Lundquist, and M. D. Dettinger (2008), Meteorological characteristics and overland precipitation impacts of atmospheric rivers affecting the West Coast of North America based on eight years of SSM/I satellite observations, *J. Hydrometeorol.*, *9*, 22–47.

Newell, R. E., N. E. Newell, Y. Zhu, and C. Scott (1992), Tropospheric rivers? A pilot study, *Geophys. Res. Lett.*, *19*, 2401–2404, doi:10.1029/92GL02916.

Newman, M., G. N. Kiladis, K. M. Weickmann, F. M. Ralph, and P. D. Sardeshmukh (2012), Relative contributions of synoptic and low-frequency eddies to time-mean atmospheric moisture transport, including the role of atmospheric rivers, *J. Clim.*, *25*, 7341–7361.

Payne, A. E., and G. Magnusdottir (2014), Dynamics of landfalling atmospheric rivers over the North Pacific in 30 years of MERRA reanalysis, *J. Clim.*, *27*, 7133–7150, doi:10.1175/JCLI-D-14-00034.1.

Pfahl, S., and H. Wernli (2008), Air parcel trajectory analysis of stable isotopes in water vapor in the eastern Mediterranean, *J. Geophys. Res.*, *113*, D20104, doi:10.1029/2008JD009839.

Pfahl, S., E. Madonna, M. Boettcher, H. Joos, and H. Wernli (2014), Warm conveyor belts in the ERA-Interim dataset (1979–2010). Part II: Moisture origin and relevance for precipitation, *J. Clim.*, *27*, 27–40.

Ploeger, F., G. Günther, P. Konopka, S. Fueglistaler, R. Müller, C. Hoppe, A. Kunz, R. Spang, J.-U. Grooß, and M. Riese (2013), Horizontal water vapor transport in the lower stratosphere from subtropics to high latitudes during boreal summer, *J. Geophys. Res. Atmos.*, *118*, 8111–8127, doi:10.1002/jgrd.50636.

Polvani, L. M., and J. G. Esler (2007), Transport and mixing of chemical air masses in idealized baroclinic life cycles, *J. Geophys. Res.*, *112*, D23102, doi:10.1029/2007JD008555.

Press, W. H., S. A. Teukolsky, W. T. Vetterling, and B. P. Flannery (1992), *Numerical Recipes in C*, 2nd ed., 1007 pp., +xxvi, Cambridge Univ. Press, New York.

Ralph, F. M., P. J. Neiman, and G. A. Wick (2004), Satellite and CALJET aircraft observations of atmospheric rivers over the eastern North Pacific Ocean during the El Niño winter of 1997/98, *Mon. Weather Rev.*, *132*, 1721–1745.

Ralph, F. M., P. J. Neiman, and R. Rotunno (2005), Dropsonde observations in low-level jets over the northeastern Pacific Ocean from CALJET-1998 and PACJET-2001: Mean vertical-profile and atmospheric-river characteristics, *Mon. Weather Rev.*, *133*, 889–910.

Ralph, F. M., P. J. Neiman, G. A. Wick, S. I. Gutman, M. D. Dettinger, D. R. Cayan, and A. B. White (2006), Flooding on California's Russian River: The role of atmospheric rivers, *Geophys. Res. Lett.*, *33*, L13801, doi:10.1029/2006GL026689.

Rienecker, M. M., et al. (2011), MERRA: NASA's Modern-Era Retrospective Analysis for Research and Applications, *J. Clim.*, *24*, 3624–3648, doi:10.1175/JCLI-D-11-00015.1.

Roca, R., J.-P. Lafore, C. Piriou, and J. L. Redelsperger (2005), Extratropical dry-air intrusions into the West African Monsoon Midtroposphere: An important factor for the convective activity over the Sahel, *J. Atmos.*, *62*, 390–407.

Ryoo, J.-M. (2009), Controls on the upper tropospheric humidity, PhD thesis, 194 pp., Johns Hopkins Univ., Baltimore, Md.

Ryoo, J.-M., D. W. Waugh, and A. Gettelman (2008), Variability of subtropical upper tropospheric humidity, *Atmos. Chem. Phys.*, *8*, 2643–2655.

Ryoo, J.-M., J.-W. Kim, E. J. Fetzer, and D. E. Waliser (2010), A study of storm tracks and the cold season precipitation characteristics in California using trajectory model, Fall Meeting, AGU, San Francisco, Calif., Dec.

Ryoo, J.-M., Y. Kaspi, D. W. Waugh, G. N. Kiladis, D. E. Waliser, E. J. Fetzer, and J. Kim (2013), Impact of Rossby Wave breaking on U.S. West Coast winter precipitation during ENSO events, *J. Clim.*, *26*, 6360–6382, doi:10.1175/JCLI-D-12-00297.1.

Schoeberl, M. R., and L. Sparling (1995), Trajectory modeling, in *Diagnostic Tools in Atmospheric Physics, Proc. Int. Sch. Phys. "Enrico Fermi,"* vol. 124, edited by G. Fiocco and G. Visconti, pp. 289–306.

Simmons, A., S. Uppala, D. Dee, and S. Kobayashi (2007), ERA-Interim: New ECMWF reanalysis products from 1989 onwards, *ECMWF Newsl.*, *110*, 1–53.

Soong, S., and J. Kim (1996), Simulation of a heavy wintertime precipitation event in California, *Clim. Change*, *32*, 55–77.

Stohl, A., G. Wotawa, P. Seibert, and H. Kromp-Kolb (1995), Interpolation errors in wind fields as a function of spatial and temporal resolution and their impact on different types of kinematic trajectories, *J. Appl. Meteorol.*, *34*, 2149–2165.

Suarez, M. J., et al. (2008), The GEOS-5 Data Assimilation System—Documentation of versions 5.0.1, 5.1.0, and 5.2.0, NASA/TM–2008–104606, 27.

Waliser, D. E., et al. (2012), The "Year" of Tropical Convection (May 2008 to April 2010): Climate variability and weather highlights, *Bull. Am. Meteorol. Soc.*, *93*(8), doi:10.1175/2011BAMS3095.1.

Waugh, D. W. (2005), Impact of potential vorticity intrusions on subtropical upper tropospheric humidity, *J. Geophys. Res.*, *110*, D11305, doi:10.1029/2004JD005664.

Waugh, D. W., and B. M. Funastu (2003), Intrusions into tropical upper troposphere: Three dimensional structure and accompanying ozone and OLR distributions, *J. Atmos. Sci.*, *60*, 637–653.

Wernli, H., and H. C. Davies (1997), A Lagrangian-based analysis of extratropical cyclones. I: The method and some applications, *Q. J. R. Meteorol. Soc.*, *123*, 467–489.

Wright, J. S., R. Fu, S. Fueglistaler, Y. S. Liu, and Y. Zhang (2011), The influence of summertime convection over Southeast Asia on water vapor in the tropical stratosphere, *J. Geophys. Res.*, *116*, D12302, doi:10.1029/2010JD015416.

Zhu, Y., and R. E. Newell (1994), Atmospheric rivers and bombs, *Geophys. Res. Lett.*, *21*, 1999–2002, doi:10.1029/94GL01710.

Zhu, Y., and R. E. Newell (1998), A proposed algorithm for moisture fluxes from atmospheric rivers, *Mon. Weather Rev.*, *126*, 725–735.